EFFECTS OF SOME AERODYNAMIC COUPLINGS, LAGS AND NONLINEARITIES ON AIRCRAFT TRAJECTORY AND DYNAMICS

by

Stephane Lucien Mondoloni

S.B., Massachusetts Institute of Technology
(1987)

Submitted to the Department of
Aeronautics and Astronautics
in Partial Fulfillment of the
Requirements for the Degree of

MASTER OF SCIENCE IN AERONAUTICS AND ASTRONAUTICS

at the

MASSACHUSETTS INSTITUTE OF TECHNOLOGY

May 1989

Signature of the Author _____
Department of Aeronautics and Astronautics, May 4, 1989

Certified by _____
Professor Eugene E. Covert
Thesis Supervisor

_____
Head of Department of Aeronautics and Astronautics

Accepted by _____
Professor Harold Y. Wachman
Chairman, Departmental Graduate Committee

EFFECTS OF SOME AERODYNAMIC COUPLINGS, LAGS AND NONLINEARITIES ON AIRCRAFT TRAJECTORY AND DYNAMICS

by

Stephane L. Mondoloni

Submitted to the Department of Aeronautics and Astronautics
on May 4, 1989, in partial fulfillment of the
requirements of the Degree of Master of Science in
Aeronautics and Astronautics

Abstract

To develop improved air superiority fighters, it is necessary to understand the high angle of attack portion of the flight envelope. This area is characterized by cross-couplings, lags and nonlinearities. A six degree of freedom simulator was completed to study the above phenomena. Frozen point wind tunnel data corresponding to an F-15 STOL Demonstrator aircraft was initially used. Modifications to the data were made to look at specific problems.

The inclusion of cross-coupling derivatives such as pitching moments due to roll and yaw rates as well as rolling and yawing moments due to pitch in a linear model yielded correct modes of motion. The most significant coupling term was the pitching moment due to roll rate.

Incorporating a model accounting for the lag in developing lift on the wing and tail modifies the short period damping. The wing lag decreases the damping whilst the tail increases it. This can be predicted with a linear model.

Discontinuities and hysterisis loops in the loads can grow to limit cycles. Other nonlinearities can have as little effect as including a second harmonic or as large an effect as yielding chaotic solutions.

Thesis Supervisor: Eugene E. Covert
Title: Professor of Aeronautics and Astronautics

ACKNOWLEDGEMENT

This is the part of the thesis where I get to say almost anything, so let me start by thanking Prof. Covert for his time, effort and patience. His ability to dredge up references to abstruse but useful publications found somewhere in the basements of the M.I.T. libraries proved indispensable and was greatly appreciated.

I thank the Charles Stark Draper Laboratory for allowing this project to be completed. Their financial support was greatly appreciated.

I will also thank all my friends at M.I.T. for lengthy conversations about life, the universe and everything. I will never eat another Chinese meal again (well maybe one or two).

I thank mom and dad for allowing me to exist. Their phone conversations definitely helped me keep some semblance of sanity.

Contents

List of Figures

List of Tables

Chapter 1
INTRODUCTION

Currently, high performance aircraft do not fully take advantage of the high angle of attack portion of the flight regime. If we are to improve upon existing aircraft, it is imperative that we understand this portion of the flight envelope. The major difficulty in understanding this flight region stems from the lateral-longitudinal coupling, the aerodynamic lags, the nonlinearities (both aerodynamical and dynamical) and the hysterisis loops.

The lateral-longitudinal coupling arises from strong forebody vortices which can assume assymetrical positions depending on the aircraft motion. This often results in relationships between the moments in one plane of motion and rates in the other plane. Another form of coupling which may occur is with angle of attack. Some slight assymetry in the design of the forebody can have a greatly amplified effect at high angles of attack. Thus, lateral forces and moments may vary with angle of attack.

Another aspect which might be important at high angles of attack is that of aerodynamic lags, specifically, the lag associated with developing lift on a surface and the time lag for wakes to convect over other aerodynamic surfaces. While this lag is also present at low angles of attack, the low speeds common in high angle of attack flight make the lags particularly long.

The equations of motion inherently contain nonlinearities in the dynamical terms. In addition, the aerodynamic terms may be nonlinearly related to the dynamical variables complicating the dynamical equations further. These nonlinearities together with the

high number of degrees of freedom make the presence of chaotic solutions possible.

More blatant nonlinearities are present when an aerodynamic surface stalls abruptly or a vortex bursts. This yields discontinuities in the forces and moments. Reattachement will require aerodynamic conditions more benign than what caused the initial separation or bursting. A hysterisis loop will be created since the value of the force or moment will depend on the history of our motion.

1.1 Objective and Approach

The purpose of this paper is to understand some of the effects on aircraft dynamics that arise from the above complications in the high angle of attack region. By using a full degree of freedom simulator with frozen point aerodynamic data, we will be able to get aircraft responses given any of the previous high angle of attack effects. Thus, we can compare simulator data to the predictions of our simple models. We have looked into the following:

- Root migration and mode shapes due to aerodynamic and dynamic cross-coupling (linear model).
- Inclusion of an aerodynamic lag model accounting for the effect of the wing's wake on the wing and tail.
- Effect of some nonlinear aerodynamics and dynamics on the aircraft time response.

Chapter 2
Motion Integrator

To get the dynamical response of an aircraft to control inputs, we used the motion integrator written by Wolf (1987). (For understanding of the simulation beyond that covered in this chapter the reader should consult Wolf (1987).) This motion integrator solves for the angular and translational velocities in a body fixed coordinate system (see figure 2).

2.1 Aerodynamic Coefficients

The aerodynamic and inertia data used corresponded to that predicted for an F-15/STOL demonstrator aircraft. These data were supplied by the Air Force Flight Dynamics Laboratory (Wright-Patterson AF base, Ohio). Although the F-15S has a close coupled canard, a canard schedule was used in the simulation to nullify the effect of the canard.

The force coefficients are acquired through lookup tables which contain cubic spline coefficients for the various force and moment coefficients. These coefficients are functions of the aerodynamic angles, rotation rates and control deflections. Although tabulated as a function of Mach number and altitude, the coefficients were assumed independent of these during each simulation (they varied less than one percent).

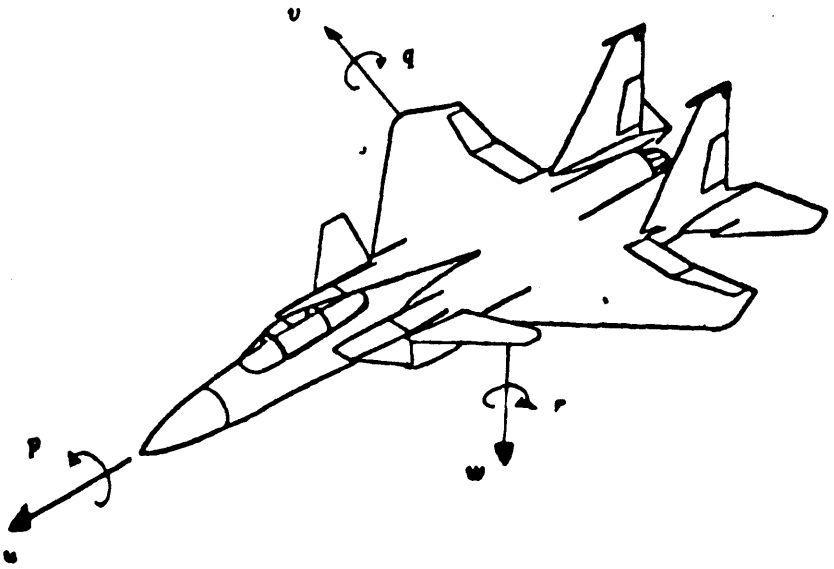

Figure 2.1: Aircraft coodinate system.

It is important to note that this lookup table approach cannot include (in the above form) any history effects. Fixing the controls, rotation rates and aerodynamic angles will always yield the same coefficients. Thus any form of hysterisis or aerodynamic lag is missing from the above model. This is significant since the high angle of attack portion of the flight envelope is characterized by strong hysterisis loops, aerodynamic lags and other history effects (ie. vortex assymetry).

2.2 Control Inputs and Trim Conditions

The simulator inputs initial conditions for all translational and rotational velocities as well as control parameters. In addition, we can input up to five rates of change (roc) of the three control surfaces and the time at which these roc's occur. The thrust is a

constant during simulations.

As initial conditions, we picked a trimmed straight and level flight condition. These trimmed conditions were determined by picking a flight angle of attack and finding the proper thrust, mass and elevator deflection which balanced the forces and moments. Thus, the mass was picked to balance the z-force, the thrust balanced the x-force and the stabilator deflection balanced the pitching moment.

2.3 Equations of Motion

The simulator solves the following equations of motion:

$$\dot{u} = vr - wq + \frac{\bar{q}S}{m}C_x - g\sin\theta \tag{2.1}$$

$$\dot{v} = wp - ur + \frac{\bar{q}S}{m}C_y + g\cos\theta\sin\phi \tag{2.2}$$

$$\dot{w} = uq - vp + \frac{\bar{q}S}{m}C_z + g\cos\theta\cos\phi \tag{2.3}$$

$$\dot{p} = \frac{-\left(\frac{I_z-I_y}{I_x} + \frac{I_{xz}^2}{I_xI_z}\right)qr + \left(1 - \frac{I_y-I_z}{I_x}\right)\frac{I_{xz}}{I_x}pq + \frac{\bar{q}Sb}{I_x}\left(C_l + \frac{I_{xz}}{I_z}C_n\right)}{1 - \frac{I_{xz}^2}{I_xI_z}} \tag{2.4}$$

$$\dot{q} = \frac{\bar{q}S\bar{c}}{I_y}C_m + \left(\frac{I_z - I_x}{I_y}\right)pr + \frac{I_{xz}}{I_y}(r^2 - p^2) \tag{2.5}$$

$$\dot{r} = \frac{\left(\frac{I_{xz}^2}{I_xI_z} - \frac{I_y-I_z}{I_z}\right)pq - \left(1 + \frac{I_z-I_y}{I_z}\right)\frac{I_{xz}}{I_z}qr + \frac{\bar{q}Sb}{I_z}\left(\frac{I_{xz}}{I_z}C_l + C_n\right)}{1 - \frac{I_{xz}^2}{I_xI_z}} \tag{2.6}$$

$$\dot{\theta} = q\cos\phi - r\sin\phi \tag{2.7}$$

$$\dot{\phi} = p + \tan\theta(q\sin\phi + r\cos\phi) \tag{2.8}$$

$$\dot{\psi} = \sec\theta(q\sin\phi + r\cos\phi) \tag{2.9}$$

$$\dot{h} = (VT)\sin\gamma \tag{2.10}$$

In addition to the above equations of motion, we require the angle of attack(α) and the sideslip angle (β) in order to retrieve the force coefficients. These are respectively:

$$\alpha = \arctan\frac{w}{u} \tag{2.11}$$

$$\beta = \arcsin\frac{v}{VT} \tag{2.12}$$

Where VT represents the total velocity.

2.4 Simulator Verification

Before using the simulator to derive aircraft trajectories, we had to be confident that the simulator was working properly. Whilst its computations had already been verified in the longitudinal plane (see Wolf, 1987), the lateral plane had not been verified. After stepping through the code and making some corrections we began by computing a three term series solution in the lateral plane to confirm that we got the proper time response. This series was computed for a Mach number of 0.6, α=1.77 deg , and 20000 feet altitude. To achieve a lateral displacement, we input a 1.5 degree rudder deflection. Our series were:

$$v = v_0 + v_1 t + v_2\frac{t^2}{2!} + v_3\frac{t^3}{3!} \tag{2.13}$$

$$r = r_0 + r_1 t + r_2\frac{t^2}{2!} + r_3\frac{t^3}{3!} \tag{2.14}$$

$$p = p_0 + p_1 t + p_2\frac{t^2}{2!} + p_3\frac{t^3}{3!} \tag{2.15}$$

From 2.8 and 2.9 this also yields (to third order):

$$\psi = \psi_0 + (r_0 t + r_1 \frac{t^2}{2!} + r_2 \frac{t^3}{3!}) \sec \theta_0 \tag{2.16}$$

$$\phi = \phi_0 + (p_0 + r_0 \tan \theta_0)t + (p_1 + r_1 \tan \theta_0)\frac{t^2}{2!} + (p_2 + r_2 \tan \theta_0)\frac{t^3}{3!} \tag{2.17}$$

We then place the above series into the lateral equations of motion and equate powers of time to get our series solution. The results for yaw rate (r) and sidelip (v) are compared to the simulator in figure 2.4. The simulator and the time series agree for small time. This gives us more confidence that the simulator is working correctly.

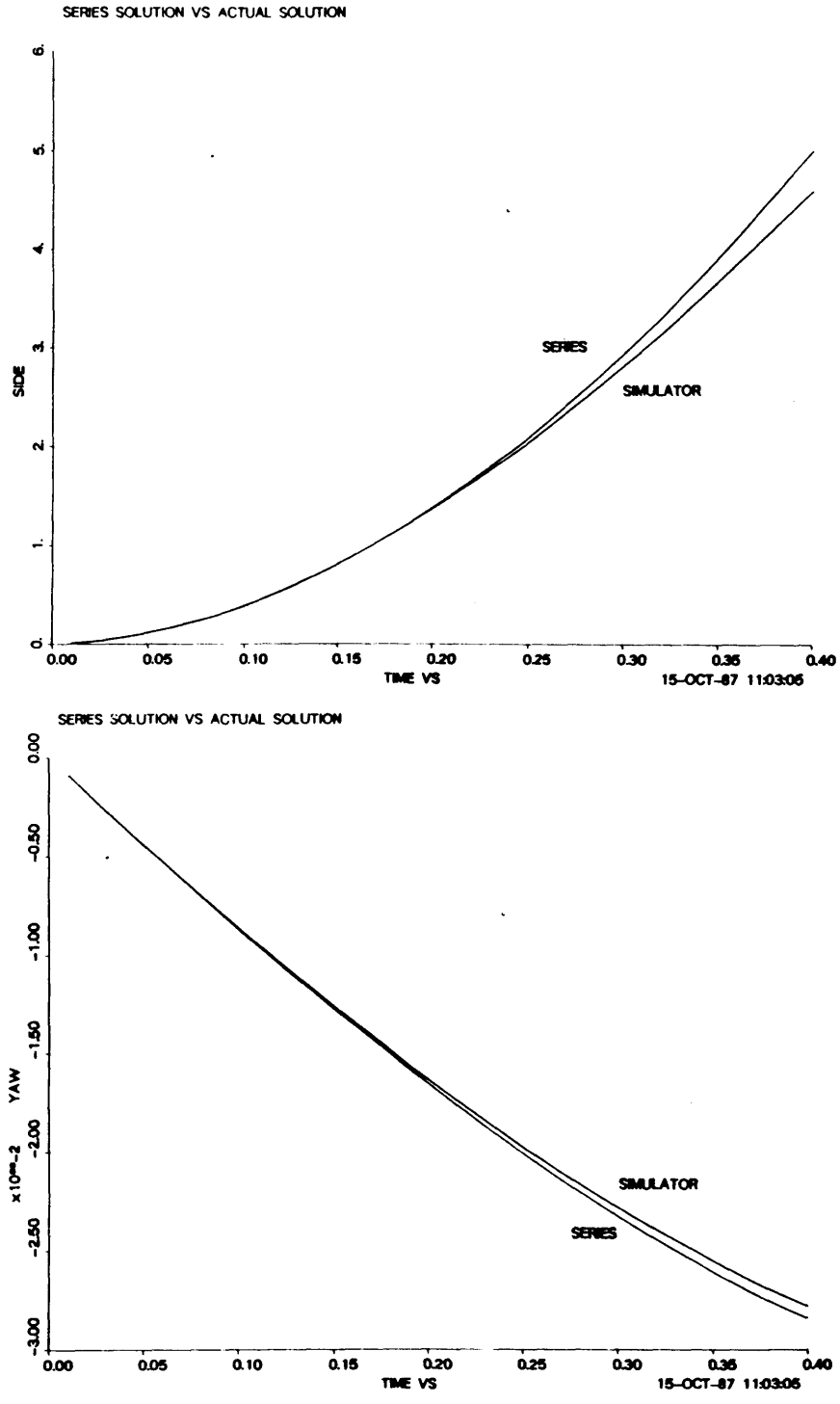

Figure 2.2: Series solution vs simulator solution

Chapter 3
Cross-Coupling

It was on December 17,1903 that the Wright brothers ushered mankind into the modern age of aviation. At about the same time work was being published by Bryan and Williams (1904) mathematically analysing the longitudinal stability of simple aeroplanes. In this work, they linearize the longitudinal equations of motion about a steady flight path. Out of such linearization naturally came the longitudinal stability derivatives as an aerodynamic representation for the aircraft. Afterwards, the lateral equations of motion were added to the aircraft mathematical model and remained uncoupled to the longitudinal equations of motion.

As aircraft got capable of higher performance, the range of angles of attack experienced by aircraft has grown. The added domain of high angles of attack introduces separation effects and strong asymmetries which require the introduction of additional stability derivatives in order to account for this aerodynamic coupling between the longitudinal and lateral planes of motion.

3.1 Justification for Addition of Cross Coupling

In the high angle of attack portion of flight, current works have shown aerodynamic coupling between the longitudinal and lateral planes of symmetry. Some authors have argued that the inclusion of such cross-coupling terms can lead to pathological perfor-

mance degradation such as wing rock, nose slice or rolling divergence.

Johnston (1978) describes wing rock as 'a predominantly rolling motion of significant amplitude'. He asserts that wing rock develops from the dutch roll mode at the point where the dynamic yawing moment due to sideslip becomes small compared with the dynamic rolling moment due to sideslip. At that point any disturbance which produces sideslip will set off a rolling oscillation. As the angle of attack is increased, the roll axis rotates toward the flight path axis and is felt by the pilot as nose slice.

In the same paper, Johnston (1978) finds that the frozen point, linear aerodynamic model was incapable of predicting wing rock whilst a simulation involving non-linear derivatives did predict wing rock felt in flight tests on an F-4. Nevertheless, he states that a frozen point, linear aerodynamic model about an asymmetric trim does lead to 'valid' predictions. Note that the aerodynamic cross coupling terms included were rolling moment due to alpha (C_{l_α}) , yawing moment due to alpha (C_{n_α}), and pitching moment due to sideslip (C_{m_β}).

Orlik-Ruckemann and Hanff (1978) presented research in which they measured cross-coupling moment derivatives of the form:

- Rolling and yawing moments due to alpha(C_{l_α} and C_{n_α})
- Pitching moment due to beta (C_{m_β})
- Pitching moment due to yaw and roll rates(C_{m_r} and C_{m_p})
- Rolling and yawing moments due to pitch rates(C_{l_q} and C_{n_q})

It is important to note that the moment derivatives due to rotation rates were significantly nonlinear with angle of attack. This nonlinearity is shown for the pitching

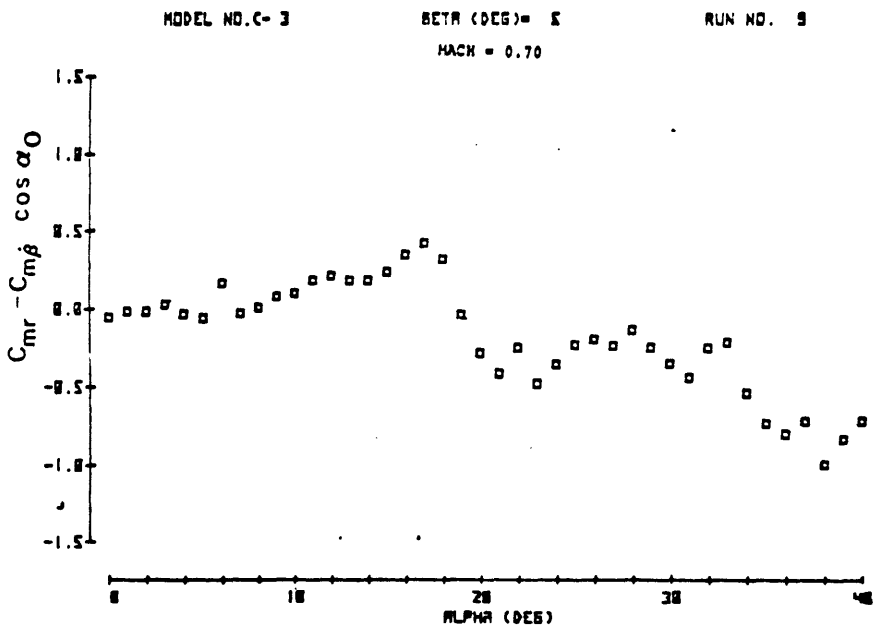

Figure 3.1: Pitching due to yaw rate derivative

moment due to yaw rate in figure 3.1 extracted from the above report.

Curry and Orlik-Ruckemann (1978) performed a dynamic simulation of a generic military fighter in steady flight as well as in a 2g turn at 33 degrees angle of attack. In the simulation they included the previously determined cross-coupling derivatives. They concluded that the most important derivatives were:

- Rolling moment due to pitch rate and change in angle of attack (C_{l_q} and $C_{l_{\dot{\alpha}}}$)
- Yawing moment due to pitch rate and change in angle of attack (C_{n_q} and $C_{n_{\dot{\alpha}}}$)

They also determined that the pitching moment due to yaw rate and sideslip rate (C_{m_r} and $C_{m_{\dot{\beta}}}$) were insignificant. The effects on aircraft response of the traditional derivatives rolling and yawing moment due to yaw rate were found to not be greater than the effects of the significant cross coupling derivatives listed above.

The above provides sufficient evidence for the existance of aerodynamic cross-coupling terms and of their subsequent significance on the aircraft flight trajectory. Our research focused on acquiring the non-dimensional equations of motion linearized about a high angle of attack flight path in order to get the aircraft modes of motion at high angles of attack. This proves useful not so much for predicting the exact flight trajectory as much as for predicting the initial (short time scales) stability to a disturbance from equilibrium. Thus, if the roots of the linearized equations of motion predict a rapid divergence, the initial motion of the aircraft will follow that prescribed path as long as the motion parameters (eg. velocities) remain small.

3.2 Linearized Equations

By non-dimensionalizing the equations of motion (equations 2.1 to 2.10) and subsequently linearizing them about a steady high angle of attack flight path, we arrive at:

$$(2\mu D - C_{x_{\dot{u}}} - 2C_{x_0}\cos\theta_0 - 2C_{x_0}\sin\theta_0\tan\theta_0)\hat{u} - (C_{x_\alpha} + 2C_{x_0}\tan\theta_0)\alpha + (2\mu\sin\theta_0 D + \frac{\mu bg}{VT0^2}\cos\theta_0)\theta = 0 \qquad (3.1)$$

$$(2\mu D - C_{Z_\alpha}\cos\theta_0 - C_{Z_{\dot{\alpha}}}\cos\theta_0 D + C_{x_\alpha}\sin\theta_0 - 2C_{Z_0}\sin\theta_0 + 2C_{x_0}\tan\theta_0\sin\theta_0)\alpha + (2C_{x_0}\sin\theta_0\cos\theta_0 - 2C_{Z_0} - C_{Z_{\dot{u}}}\cos\theta_0 + C_{x_{\dot{u}}}\sin\theta_0 + 2C_{x_0}\tan\theta_0\sin\theta_0{}^2)\hat{u} - (2\mu D + C_{Z_q}\cos\theta_0 D)\theta = 0 \qquad (3.2)$$

$$-C_{m_{\dot{u}}}\hat{u} - (C_{m_\alpha} + C_{m_{\dot{\alpha}}}D)\alpha + (i_B\frac{\bar{b}}{\bar{c}}D^2 - C_{m_q}D)\theta - C_{m_\beta}\beta - C_{m_p}D\phi + (C_{m_p}\tan\theta_o - C_{m_r})r = 0 \qquad (3.3)$$

$$-C_{y_\alpha}\alpha + (2\mu D - C_{y_\beta})\beta - (2\mu\sin\theta_0 D + C_{y_p}D + \mu\frac{bg}{VT0^2}\cos\theta_0)\phi + (2\mu\cos\theta_0 + 2\mu\sin\theta_0\tan\theta_0 - C_{y_r} + C_{y_p}\tan\theta_0)r = 0 \qquad (3.4)$$

$$-C_{l_\alpha}\alpha - C_{l_q}D\theta - C_{l_\beta}\beta + (i_A D^2 - C_{l_p}D)\phi$$
$$+(C_{l_p}\tan\theta_0 - C_{l_r} - i_A \tan\theta_0 D - i_E D)r = 0 \tag{3.5}$$

$$-C_{n_\alpha}\alpha - C_{n_q}D\theta - C_{n_\beta}\beta - (i_E D^2 + C_{n_p}D)\phi$$
$$+(i_C D + i_E \tan\theta_0 D + C_{n_p}\tan_{\theta_0} - C_{n_r})r = 0 \tag{3.6}$$

For a detailed derivation of the above equations, the reader should consult appendix A. Note that in the above case, all equations were non-dimesionalized by using half the wingspan as a length.

3.3 Verifying Roots

A first check on the above equations is that they reduce to the linear equations for straight and level flight when θ is set to zero. Clearly they do reduce to those equations given in Etkin(1982).

We then wrote a code to solve for the above eigenvalues and corresponding modes when input the stability derivatives computed from the simulator data. For a trim at forty degrees angle of attack, we get the modes shown in figure 3.2. Note their periods and half times are given by Table 3.1.

The table compares the periods and half-times predicted by the linearized roots to the results from a simulation trimmed for 40 degrees angle of attack. Note that the predominance of the dutch roll in the lateral variables and similarly the short period in the longitudinal variables, makes determination of the period and half-times of the phugoid and second lateral mode difficult. I believe that the reason for the dutch roll half time being far off is predominantly due to the nonlinearity in the sideforce due to sideslip (C_{y_β}) see figure 3.3. Note that the predominant effect of varying C_{y_β} is to modify the dutch roll damping (Figure 3.4).

	Linear Roots		Simulator	
Mode	Period(sec)	Half-time	Period(sec)	Half-Time
Phugoid	37.20	12.14	—	—
Other Lat	73.65	4.46	—	—
Short	4.63	2.43	4.6	2.3
Dutch	2.36	2.63	2.4	3.1

Table 3.1: Period and half-times of linear model vs simulator.

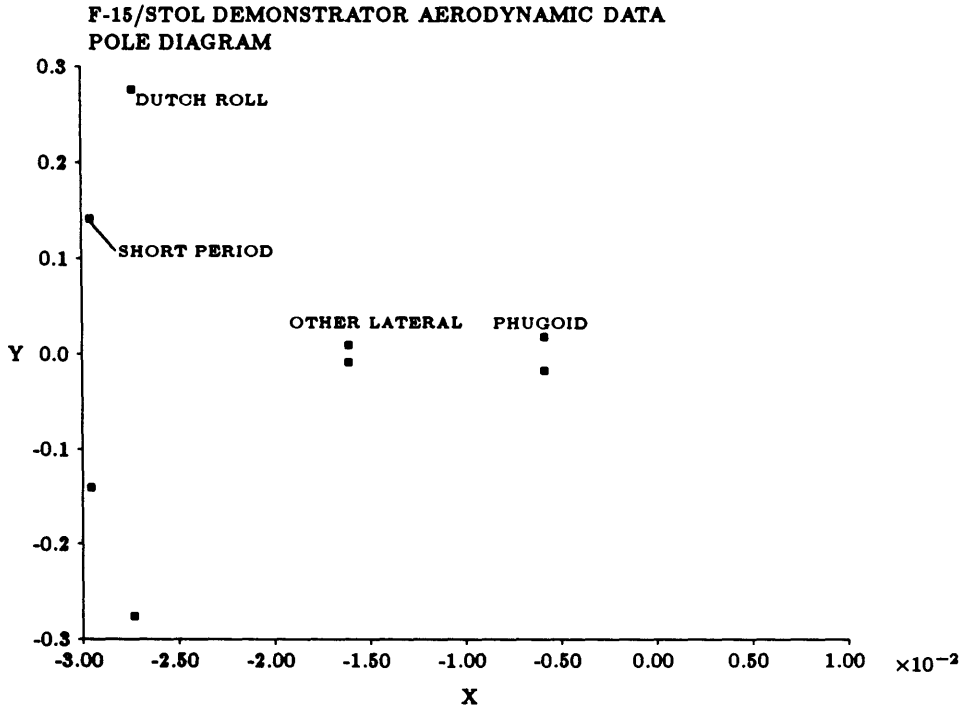

Figure 3.2: Modes at 40 degrees AOA.

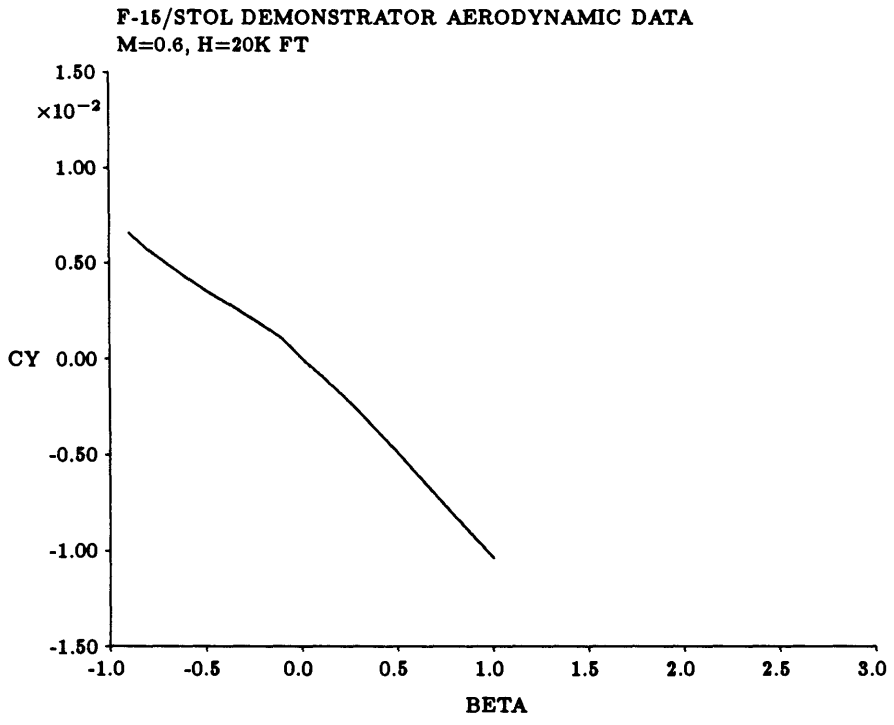

Figure 3.3: Sideforce coefficient versus sideslip angle in degrees.

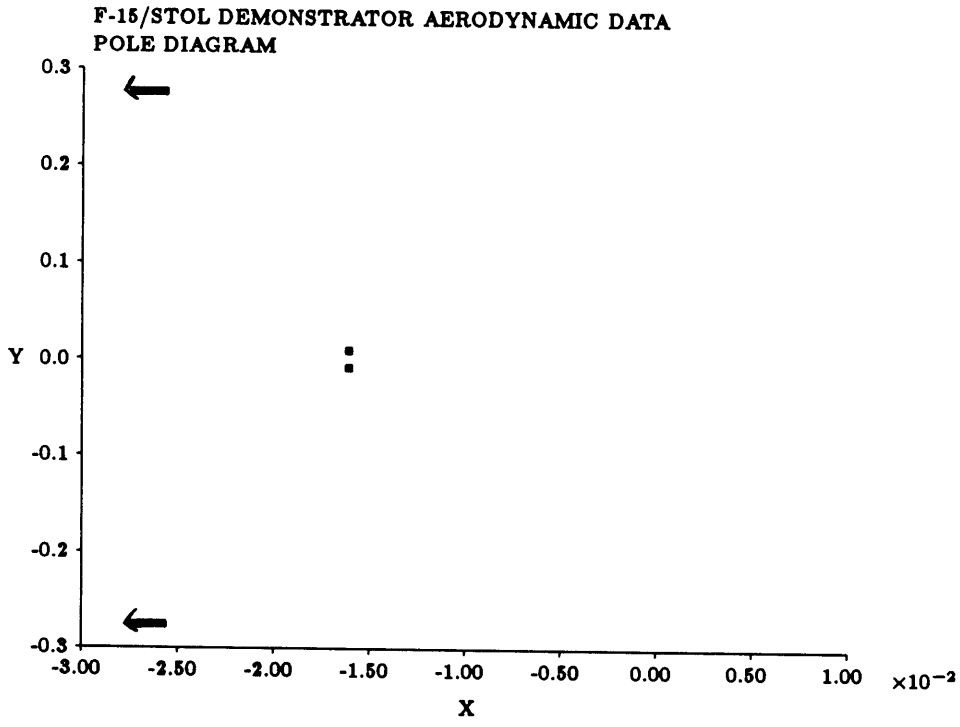

Figure 3.4: Lateral root migration for C_{y_β} =0 to -.6

	Linear Roots		Simulator	
Mode	Period(sec)	Half-time	Period(sec)	Half-Time
Other Lat	73.20	4.57	—	4.38
Dutch	2.34	1.33	2.35	1.34

Table 3.2: Periods and half-times for lateral roots given increased C_{y_β}.

	Linear Roots		Simulator	
Mode	Period(sec)	Half-time	Period(sec)	Half-Time
Phugoid	39.02	12.53	37.2	14.8

Table 3.3: Phugoid periods and half-times for large C_{m_q}.

In order to 'see' the other lateral mode better we artificially set the sideforce due to sidelip coefficient (C_{y_β}) such that the dutch roll would damp out quickly. From this, the lateral roots give us the periods and half-times in Table 3.2. Note that the heavy damping of the lateral mode does not allow us to get the period from the time response. However, we see that the linear sideforce due to sideslip does give us a better half-time for the Dutch roll.

To verify the phugoid motion, we set the damping in pitch term (C_{m_q}) to be -20 from -6.1 . This quickly damps out the short period mode. Our simulations yield a good agreement in period and worst agreement in half-time as shown in Table 3.3.

We see that the previous linearized equations will predict the high angle of attack root locations. As an added benefit, the above provides yet another check on the simulator results as well.

3.3.1 Mode Shapes

The modes encountered at high angle of attack in our case were:

Term(magnitude)	Short	Phugoid	Term(magnitude)	Dutch	Lateral 2
$\frac{\hat{u}}{\theta}$	0.63	0.67	$\frac{\hat{u}}{\phi}$	0.00	0.00
$\frac{\alpha}{\theta}$	1.01	0.03	$\frac{\alpha}{\phi}$	0.00	0.00
$\frac{\beta}{\theta}$	0.00	0.00	$\frac{\theta}{\phi}$	0.00	0.00
$\frac{\phi}{\theta}$	0.00	0.00	$\frac{\beta}{\phi}$	0.63	0.01
$\frac{\psi}{\theta}$	0.00	0.00	$\frac{\psi}{\phi}$	0.02	0.33

Table 3.4: Shapes of modes from linear model (40 degrees AOA).

- A low frequency phugoid mode which is mostly a x-velocity ($\hat{u}$) and pitch angle (θ) oscillation.
- A short period mode which is an oscillation in all longitudinal variables.
- A dutch roll mode which is an oscillation in sideslip (β) and bank angle (ϕ) with little variation in non-dimensionalized roll rate. Their is some heading oscillation (15 percent).
- An overly damped oscillation in roll which is primarily a convergence in heading angle(ψ) with some convergence in bank angle (ϕ), one can think of this mode as a combination rolling convergence and stable spiral mode.

The shapes of the modes are summarized in Table 3.4.

These modes were verified through simulation. For instance, in a simulation the ratio of the magnitudes of beta and phi was found to average 0.63 when the motion was predominated by the dutch roll. We compare beta to 63 percent of phi in figure 3.5. Note that phi includes some of the second lateral oscillation and hence drifts away from beta.

3.4 Root Migration with Cross-Coupling

By adding in selected cross-coupling terms, we determined the motion of the roots and the change in the shape of the modes. From the F-15S data, we had the following asymmetric terms:

- Sideforce due to angle of attack, $C_{y_\alpha} = .4098$
- Yawing moment due to angle of attack, $C_{n_\alpha} = -.00058$
- Rolling moment due to angle of attack, $C_{l_\alpha} = .00191$

We then added the following combination of terms:

- C_{n_q} with C_{m_r}.
- C_{l_q} with C_{m_r}.
- C_{n_q} with C_{m_p}.
- C_{l_q} with C_{m_p}.

Note that we needed terms forcing the lateral equations and terms forcing the longitudinal equations to get some feedback between the modes. This feedback interrelates the modes such that there is some variation in shape and root location. Had we simply included the lateral terms (C_{l_q} and C_{n_q}) then we could solve for the longitudinal equations independently and consider them as forcing functions to the lateral equations.

Term(magnitude)	Short	Phugoid	Term(magnitude)	Dutch	Lateral 2
$\frac{q}{\theta}$	0.63	0.64	$\frac{q}{\phi}$	0.001	0.004
$\frac{\alpha}{\theta}$	1.01	0.04	$\frac{\alpha}{\phi}$	0.001	0.003
$\frac{\beta}{\theta}$	0.09	0.05	$\frac{\theta}{\phi}$	0.001	0.001
$\frac{\phi}{\theta}$	0.63	3.58	$\frac{\beta}{\phi}$	0.63	0.01
$\frac{\psi}{\theta}$	0.35	2.74	$\frac{\psi}{\phi}$	0.02	0.33
$\frac{p}{\theta}$	0.04	0.04	$\frac{p}{\phi}$	0.003	0.005

Table 3.5: Mode shapes for C_{n_q}=1 and C_{m_q}=1.

3.4.1 Effects of pitching moment due to yaw rate with yawing moment due to pitch rate

We included a pitching moment due to yaw rate (equal to 1.) and found the subsequent motion of the roots as we vary the yawing moment due to pitch rate from -1 to 1 (shown in Figure 3.6). Clearly, the effect on the location of the roots is small.

Nevertheless, the shape of the roots is significantly modified. Table 3.5 illustrates the relative magnitude of terms in the various modes (for $C_{n_q} = 1$). Although the lateral modes do not change much from the uncoupled case (see Table 3.4) except that now we have very slight longitudinal components, the longitudinal modes include significant lateral oscillations. The short period and phugoid include noticeable variations in bank angle (ϕ) and heading angle (ψ).

As a short period mode is excited, this causes rolling moment (due to the pitch rate through C_{n_q} and angle of attack through C_{n_α}) as well as sideforce (from C_{y_α}) oscillations at the short period frequency. The oscillations in yaw subsequently excite pitching through C_{m_r}. However, the excitations in yaw rate are not large enough (4 percent) to significantly force the pitching moment. This lack of feedback explains why the roots do not undergo significant motion. Since bank and heading are integrated

Term(magnitude)	Short	Phugoid	Term(magnitude)	Dutch	Lateral 2
$\frac{u}{\theta}$	0.63	0.68	$\frac{u}{\phi}$	0.001	0.004
$\frac{\alpha}{\theta}$	1.01	0.03	$\frac{\alpha}{\phi}$	0.001	0.003
$\frac{\beta}{\theta}$	0.49	0.05	$\frac{\theta}{\phi}$	0.001	0.001
$\frac{\phi}{\theta}$	0.90	0.77	$\frac{\beta}{\phi}$	0.63	0.01
$\frac{\psi}{\theta}$	0.08	0.51	$\frac{\psi}{\phi}$	0.02	0.33

Table 3.6: Mode shapes for C_{l_q}=1 and C_{m_r}=1 .

values of roll and yaw, they are large components of the short period mode.

Similarly, since the phugoid is initially an oscillation in incidence angle (θ) and x-velocity, the phugoid forces the lateral components mostly through C_{n_q} (recalling that $q = \dot{\theta}$ for small values). Once again their is not much motion of the roots since the yaw rate is small.

The fact that the yaw rate is small in all modes, signifies that the lateral modes do not have as large an effect on the longitudinal modes (by action of C_{m_r}) as the longitudinal modes have on the lateral modes.

3.4.2 Effects of pitching moment due to yaw rate with rolling moment due to pitch rate

Keeping the same pitching moment due to yaw rate as above, we now varied the rolling moment due to pitch rate (C_{l_q}) from -1 to 1. This yielded the root movement shown in Figure 3.7 and the modes shown (at $C_{l_q} = 1$) in Table 3.6 .

We note that the lateral modes did not vary much from the previous case (see Table 3.5). The reason for this is that the lateral modes affect the longitudinal variables through C_{m_r} which is the same as before.Since the longitudinal variables are not excited

much through C_{m_r}, they do not have much counter effect on the lateral variables through C_{l_q}. Thus we can consider the lateral modes as small forcing functions of the longitudinal variables.

As before, the short period significantly excites the bank angle. We note that C_{l_q} excites the sideslip (β) more than C_{n_q} in the short period mode and also excites the heading angle (ψ) less. The direct effect of C_{n_q} is no longer present, thus the heading angle is less affected by pitch rates. However, sideslip effect is increased since the much smaller yaw rate (since C_{n_q} is no longer present) no longer offsets the C_{y_α} term (see equation 3.4). Hence sideslip encounters more forcing than before. Our short period now looks like a combination short period and dutch roll oscillation.

The phugoid oscillation contains less variation in heading and bank angle than before. This is due to less effect on yaw through C_{n_q} which integrates into both ϕ and ψ. Roll (through C_{l_q}) only integrates directly into ϕ.

3.4.3 Effects of pitching moment due to roll rate with yawing moment due to pitch rate

When we only included $C_{m_p} = 1$ and varied C_{n_q} from -1 to 1, we got the root motion shown in figure 3.8. The shapes for $C_{n_q} = 1$ are given by Table 3.7 .

Note that we get much more coupling effect with the rolling term (C_{m_p}) than with C_{m_r} (see Table 3.5), this is due to the roll rates being larger than the yaw rates (by a factor of about 80 in the dutch roll and 4 in the second lateral mode). The mechanism through which the root location is modified can be understood by looking at the frequency response diagrams of pitch and roll. When we excite the longitudinal variables at the dutch roll frequency and damping, we get the frequency response in q shown in figures 3.9 and 3.10. This results in mostly an oscillation in q at 61.3 degrees phase lag

Term(magnitude)	Short	Phugoid	Term(magnitude)	Dutch	Lateral 2
$\frac{q}{\theta}$	0.63	0.65	$\frac{q}{\phi}$	0.05	0.02
$\frac{\alpha}{\theta}$	1.01	0.01	$\frac{\alpha}{\phi}$	0.07	0.01
$\frac{\beta}{\theta}$	0.09	0.05	$\frac{\theta}{\phi}$	0.07	0.003
$\frac{\phi}{\theta}$	0.63	3.76	$\frac{\beta}{\phi}$	0.64	0.01
$\frac{\psi}{\theta}$	0.35	2.79	$\frac{\psi}{\phi}$	0.01	0.32

Table 3.7: Shape of modes with C_{m_p}=1 and C_{n_q}=1 .

Term(magnitude)	Short	Phugoid	Term(magnitude)	Dutch	Lateral 2
$\frac{q}{\theta}$	0.64	0.68	$\frac{q}{\phi}$	0.05	0.02
$\frac{\alpha}{\theta}$	1.02	0.04	$\frac{\alpha}{\phi}$	0.08	0.01
$\frac{\beta}{\theta}$	0.53	0.05	$\frac{\theta}{\phi}$	0.08	0.003
$\frac{\phi}{\theta}$	0.96	0.71	$\frac{\beta}{\phi}$	0.62	0.01
$\frac{\psi}{\theta}$	0.07	0.51	$\frac{\psi}{\phi}$	0.02	0.33

Table 3.8: Mode shapes for C_{m_p}=1 and C_{l_q}=1.

to p. When we then force the roll through C_{n_q} (using the largest response from above) we get the response in p which is shown in figures 3.11 and 3.12. Note that the response at the dutch roll frequency is increased in magnitude but is exactly 180 degrees out of phase with the initial excitation (in p). This feedback of q cancels the initial excitation in p thereby increasing the damping (moving the root to the left). Similar arguments can be used to explain the other root motions but quickly get reduntant.

3.4.4 Effects of pitching moment due to roll rate with rolling moment due to pitch rate

We now included C_{m_p} as before but varied C_{l_q} from -1 to 1 and got the root motion shown in figure 3.13. The mode shapes are given by (for $C_{l_q} = 1$) Table 3.8 . Once

again, we get significant cross-coupling (due to C_{m_p}). The dutch roll and short period modes undergo a significant change in damping. The dutch roll is destabilized with positive C_{m_p} and C_{l_q} while the short period is stabilized.

To observe the cross-coupling effect in the simulation, we show a comparison of sideslip with and without the above coupling (Figure 3.14). The case shown is the response to a 5 degree aileron pulse for the aircraft trimmed at 40 degrees angle of attack. The curves show the decreased damping in dutch roll as well as a slight decrease in frequency. The change in damping is much greater than that predicted by the above linear model. This doesn't cause concern since the linear model did not get the true dutch roll damping without coupling (due to the nonlinear C_{y_β} explained before). We observe that initially the damping in sideslip appears slightly negative. Also, the cross-coupled sideslip includes some component of the short period mode (which is at roughly half the frequency of the dutch roll).

A comparison of the response in angle of attack (to an initial angle) shows that the cross-coupling increases the damped frequency and increases the damping. Curve fitting reveals a 2.3 percent increase in damped frequency and 6 percent increase in damping from the uncoupled simulation. The linear model predicts a 4.7 percent increase in damped frequency and 8.7 percent increase in damping. Our linear model predicts the proper trends. Since the changes in time response due to the coupling were taken from curve fitting, and since the changes are relatively small, we believe the linear model to be a good predictor of the coupling effect (considering the small displacements).

3.5 Dynamical Coupling in a Turn

When an aircraft is performing a turn, the roll, pitch and yaw rates combine in the equations of motion to dynamically couple the longitudinal and lateral variables.

The presence of a bank angle also couples the modes. To see the effect of this type of coupling on the aircraft linearized stability, we linearized the equations of motion about a coordinated turn at high angle of attack. The conditions for a coordinated turn were as follows:

1. No change in pitch angle, given by:

$$\hat{q}_0 = \hat{r}_0 \tan \phi_0 \tag{3.7}$$

2. No change in bank angle, signifying:

$$\hat{p}_0 = -\tan \theta_0 (\hat{r}_0 \cos \phi_0 + \hat{q}_0 \sin \phi_0) \tag{3.8}$$

3. A constant roll and yaw rate:

$$C_{l_0} = (i_C - i_B)\hat{q}_0\hat{p}_0 - i_E\hat{p}_0\hat{q}_0 \tag{3.9}$$

$$C_{n_0} = (i_B - i_A)\hat{q}_0\hat{p}_0 + i_E\hat{r}_0\hat{q}_0 \tag{3.10}$$

4. A constant pitch rate:

$$C_{m_0} = (i_A - i_C)\hat{p}_0\hat{r}_0 - i_E(\hat{r}_0{}^2 - \hat{p}_0{}^2) \tag{3.11}$$

5. No change in velocities:

$$C_{x_0} = \frac{\mu g b}{(VT0)^2} \sin \theta_0 + 2\mu \hat{q}_0 \sin \theta_0 \tag{3.12}$$

$$C_{y_0} = -\frac{\mu g b}{(VT0)^2} \cos \theta_0 \sin \phi_0 + 2\mu(\hat{r}_0 \cos \theta_0 - \hat{p}_0 \sin \theta_0) \tag{3.13}$$

$$C_{z_0} = -\frac{\mu g b}{(VT0)^2} \cos \theta_0 \cos \phi_0 + 2\mu \hat{q}_0 \cos \theta_0 \tag{3.14}$$

The first three conditions relate the angular velocities once a pitch angle has been specified. The subsequent equations determine the bank angle, thrust, control surface deflections(3) and mass once a roll rate and pitch angle have been specified.

To linearize the equations of motion about a coordinated turn for high angle of attack (equal to the euler angle θ_0 in our equations), we include roll (p_0), pitch (q_0), and yaw (r_0) rates as well as a bank angle (ϕ_0). This yields the following equations of motion:

$$\begin{aligned}(2\mu D - C_{x_{\dot{u}}} - 2C_{x_0}\cos\theta_0 + 2\mu\hat{q}_0\tan\theta_0 - 2C_{x_0}\sin\theta_0\tan\theta_0)\hat{u} \\ -(C_{x_\alpha} + 2C_{x_0}\tan\theta_0 - 2\mu\hat{q}_0\sec\theta_0)\alpha + 2\mu\sin\theta_0\hat{q} \\ +(\frac{\mu bg}{VT0^2}\cos\theta_0)\theta - 2\mu\hat{r}_0 = 0 \end{aligned} \tag{3.15}$$

$$\begin{aligned}(2\mu D - C_{Z_\alpha}\cos\theta_0 - C_{Z_{\dot{\alpha}}}\cos\theta_0 D + C_{x_\alpha}\sin\theta_0 - 2C_{Z_0}\sin\theta_0 + 2C_{x_0}\tan\theta_0\sin\theta_0)\alpha \\ -2\mu\hat{q}_0\tan\theta_0\alpha + (2C_{x_0}\sin\theta_0\cos\theta_0 - 2C_{Z_0} - C_{Z_{\dot{u}}}\cos\theta_0 + C_{x_{\dot{u}}}\sin\theta_0)\hat{u} \\ +(2C_{x_0}\tan\theta_0\sin{\theta_0}^2 - 2\mu\hat{q}_0(\cos\theta_0 + \sin\theta_0\tan\theta_0))\hat{u} - (2\mu + C_{Z_q}\cos\theta_0)\hat{q} \\ +\frac{\mu gb}{VT0^2}(\sin\theta_0\cos\theta_0\cos\phi_0 - \cos\theta_0\sin\theta_0)\theta \\ +2\mu(\hat{p}_0\cos\theta_0 + \hat{r}_0\sin\theta_0)\beta + \frac{\mu gb}{VT0^2}(\cos{\theta_0}^2\sin\phi_0)\phi = 0 \end{aligned} \tag{3.16}$$

$$\begin{aligned}(-2C_{x_0}\cos\theta_0 - 2C_{x_0}\sin\theta_0\tan\theta_0 - C_{m_{\dot{u}}})\hat{u} - (C_{m_\alpha} + C_{m_{\dot{\alpha}}}D - 2C_{m_0}\tan\theta_0)\alpha \\ +(i_B\frac{\bar{b}}{\bar{c}}D - C_{m_q})\hat{q} - C_{m_\beta}\beta + (\frac{\bar{b}}{\bar{c}}(i_A - i_C)\hat{r}_0 + 2\frac{\bar{b}}{\bar{c}}i_E\hat{p}_0 - C_{m_p})\hat{p} \\ +(\frac{\bar{b}}{\bar{c}}(i_A - i_C)\hat{p}_0 - 2\frac{\bar{b}}{\bar{c}}i_E\hat{r}_0 - C_{m_r})\hat{r} = 0 \end{aligned} \tag{3.17}$$

$$-(\cos\phi_0)\hat{q} + D\theta + (\sin\phi_0)\hat{r} + (\hat{q}_0\sin\phi_0 + \hat{r}_0\cos\phi_0)\phi = 0 \tag{3.18}$$

$$\begin{aligned}(-2C_{y_0}\cos\theta_0 - 2C_{y_0}\sin\theta_0\tan\theta_0 + 2\mu\hat{r}_0 - 2\mu\hat{p}_0\tan\theta_0)\hat{u} \\ (-2\mu\hat{p}_0\sec\theta_0 - 2C_{y_0}\tan\theta_0 - C_{y_\alpha})\alpha + (\frac{\mu bg}{VT0^2}\sin\theta_0\sin\phi_0)\theta + (2\mu D - C_{y_\beta})\beta \\ -(2\mu\sin\theta_0 + C_{y_p})\hat{p} + (2\mu\cos\theta_0 - C_{y_r})\hat{r} - (\frac{\mu bg}{VT0^2}\cos\theta_0\cos\phi_0)\phi = 0 \end{aligned} \tag{3.19}$$

$$
\begin{aligned}
&(-2C_{l_0}\cos\theta_0 - 2C_{l_0}\sin\theta_0\tan\theta_0)\hat{u} \\
&-(2C_{l_0}\tan\theta_0 + C_{l_\alpha})\alpha + ((i_C - i_B)\hat{r}_0 - i_E\hat{p}_0 - C_{l_q})\hat{q} \\
&-C_{l_\beta}\beta + (i_A D - C_{l_p} - i_E\hat{q}_0)\hat{p} + ((i_C - i_B)\hat{q}_0 - C_{l_r} - i_E D)\hat{r} = 0
\end{aligned} \tag{3.20}
$$

$$
\begin{aligned}
&(-2C_{n_0}\cos\theta_0 - 2C_{n_0}\sin\theta_0\tan\theta_0)\hat{u} \\
&-(2C_{n_0}\tan\theta_0 + C_{n_\alpha})\alpha + ((i_B - i_A)\hat{p}_0 + i_E\hat{r}_0 - C_{n_q})\hat{q} \\
&-C_{n_\beta}\beta + ((i_B - i_A)\hat{q}_0 - C_{n_p} - i_E D)\hat{p} + (i_C D - C_{n_r} + i_E\hat{q}_0)\hat{r} = 0
\end{aligned} \tag{3.21}
$$

$$
\begin{aligned}
&-\sec\theta_0{}^2(\hat{q}_0\sin\phi_0 + \hat{r}_0\cos\phi_0)\theta - (\sin\phi_0\tan\theta_0\hat{q} \\
&-\hat{p} - (\cos\phi_0\tan\theta_0)\hat{r} + (D + \hat{r}_0\sin\phi_0\tan\theta_0 - \hat{q}_0\cos\phi_0\tan\theta_0)\phi = 0
\end{aligned} \tag{3.22}
$$

By looking at the above equations for small trim angles of attack ($\theta_0 = 0$), we can see the effects of a bank angle (ϕ_0) on the roots. We will for now neglect the rotation rates. As bank is increased, our pitch angle is less dependent on pitch rate as follows:

$$D\theta = \hat{q}\cos\phi_0 \tag{3.23}$$

The effect of this is to increase the short period frequency (through the $C_{Z_q}\cos\theta_0 + 2\mu$ term combined with $i_B D - C_{m_q}$). Recalling that our short period damping is approximately given by:

$$\zeta = -\frac{2\mu C_{m_q} + i_B C_{Z_\alpha} + 2\mu C_{m_{alpha}}}{2\sqrt{2\mu i_B(C_{Z_\alpha}C_{m_q} - 2\mu C_{m_\alpha})}} \tag{3.24}$$

One term decreases the short period damping (C_{m_q} becomes $C_{m_q}\cos\phi_0$) whilst another term (i_B becomes $i_B\cos\phi_0$) increases the damping. Thus, the effect on short period damping is dependent on the magnitude of terms. The same term which affects the short period frequency also decreases the phugoid damping.

Term(magnitude)	Dutch	Short	Phugoid	Roll	Spiral
$\frac{\hat{u}}{\phi}$	.003	0.59	0.23	.05	8.01
$\frac{\alpha}{\phi}$	.008	1.00	0.04	.03	1.27
$\frac{\hat{q}}{\phi}$	.002	0.14	0.01	.01	0.31
$\frac{\theta}{\phi}$	.003	0.21	0.77	.18	6.85
$\frac{\beta}{\phi}$	.600	0.06	0.01	.01	0.21
$\frac{\hat{p}}{\phi}$	.270	0.05	0.01	.03	0.04
$\frac{r}{\phi}$	.010	0.01	0.01	.03	0.26
$\frac{\psi}{\phi}$	.022	1.15	0.96	.01	14.21

Table 3.9: Shapes of modes for aircraft in 74 degree bank at 40 degress AOA.

3.5.1 Root motion

We found trim conditions coordinated turns at a Mach number of 0.2 with forty degrees angle of attack. These trim conditions were for rotation rates of 0.05,0.1,0.15 and 0.2 radians per second. Note that at forty degrees angle of attack, these rates correspond to 24, 45, 62 and 74 degrees of bank angle. By solving for the roots using the linearized equations, we got the root motion from straight and level shown in figure 3.16. The short period roots get damped significantly more under the turn. The dutch roll roots do not move significantly. The phugoid is less damped as predicted before and the second lateral mode split up into the more conventional spiral instability and rolling convergence mode.

At 74 degrees of bank angle, we computed the shapes of the various modes. These are shown in Table 3.9 .

The dynamic coupling in the turn changes the dutch roll shape very little (see Table 3.4). The short period now has significant heading variation (ψ) and it appears as though the shape of the mode is close to the unbanked case with heading angle replacing the

pitch angle (like a short period oscillation sideways). The phugoid undergoes significant variation in location and shape. The unstable phugoid is now primarly a growing oscillation in bank, heading and pitch angle as well as a smaller oscillation in x-velocity. To show the combinations of all angles, the phugoid mode is shown in figure 3.17 starting from a pertubation from our coordinated turn. The rolling convergence mode is just a decay in bank angle. The spiral mode is now a growing exponential in heading and pitch angle with growing x-velocity.

When we ran a simulation for the above trim condition, the unstable modes began to grow and we could not get a truly trimmed turn. We note that beginning with just our trim case (no control disturbances), we got the x-velocity shown in figure 3.18. This is almost a pure exponential growth with double-time of 1.9 seconds. We see that this is the spiral instability manifesting itself in the x-velocity since our linear model predicts a double time of 2.1 seconds.

We input an 5 degree elevator pulse to see the other modes which were present. The angle of attack oscillates with a period of 4.3 seconds instead of the predicted 4.4 seconds. We cannot tell the damping in angle of attack since it is combined with another slowly varying mode (see Figure 3.19). The motion in bank angle is predominantly a growing oscillation (our new phugoid) with period 30 seconds (linear model predicts 32.2 seconds) and double time of 10.0 seconds (linear model predicts 9.6 seconds). The bank angle is shown in figure 3.20. The dutch roll is not a significant component of the motion, nevertheless, oscillations in sideslip of period 2.1 seconds do occur (linear model predicts 2.3 seconds).

Despite the strong couplings that do occur, as long a we linearize about our turn state, the linearized model is a good predictor of the fundamental modes of motion. Even though we were trimmed at a high angles of bank and attack, the nonlinearities occuring during the above maneuver were not significant enough to drastically alter the predominant linear motion.

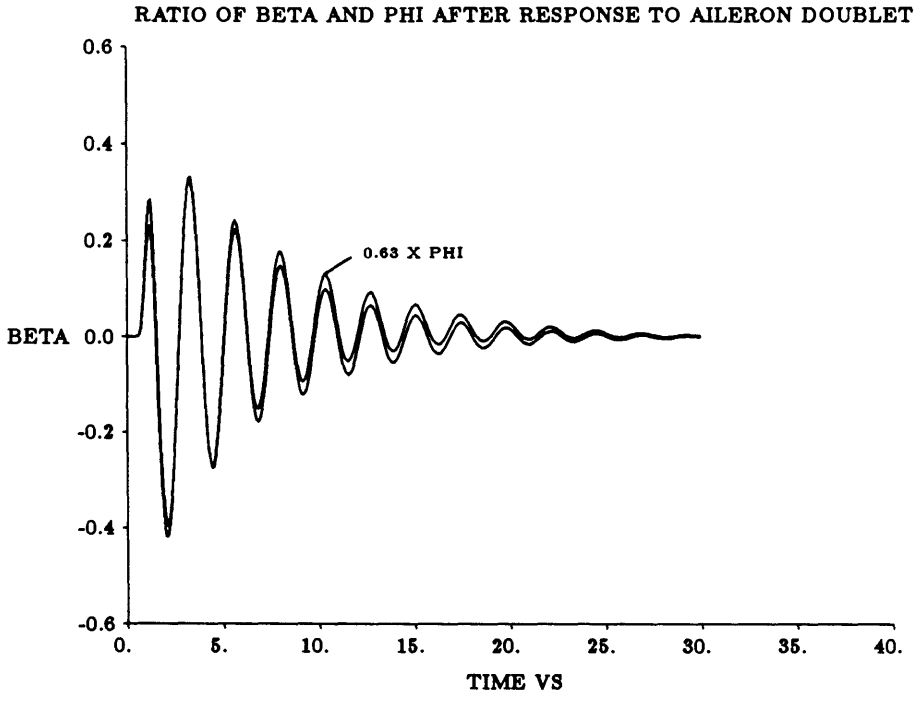

Figure 3.5: Comparison of beta to 63 percent of phi to check shape of dutch roll.

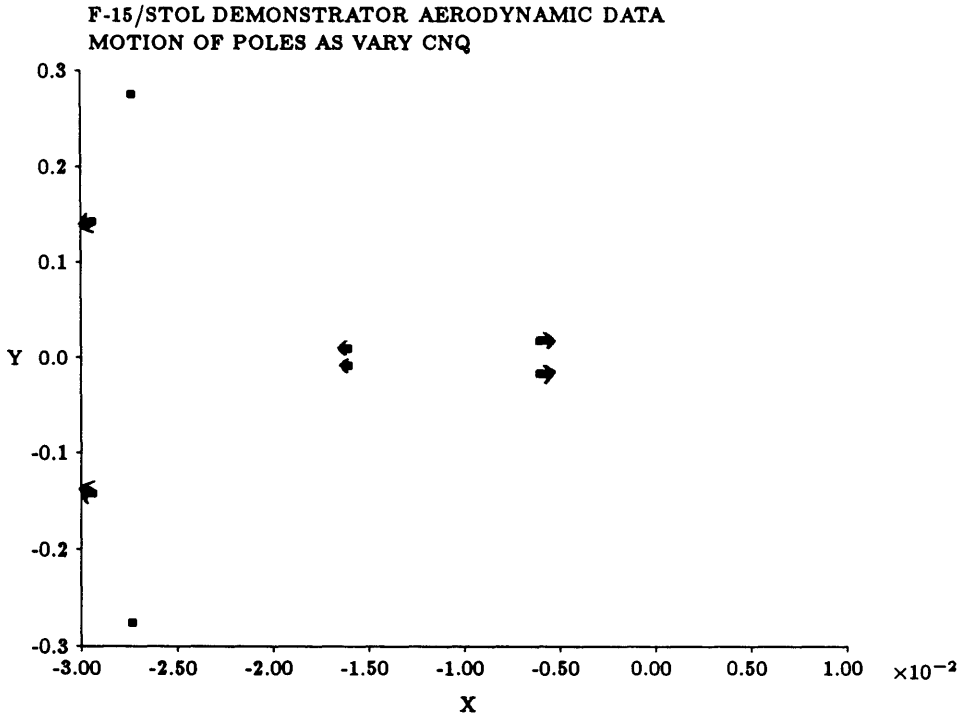

Figure 3.6: Root migration $C_{m_r} = 1$ and C_{n_q} = -1 to 1

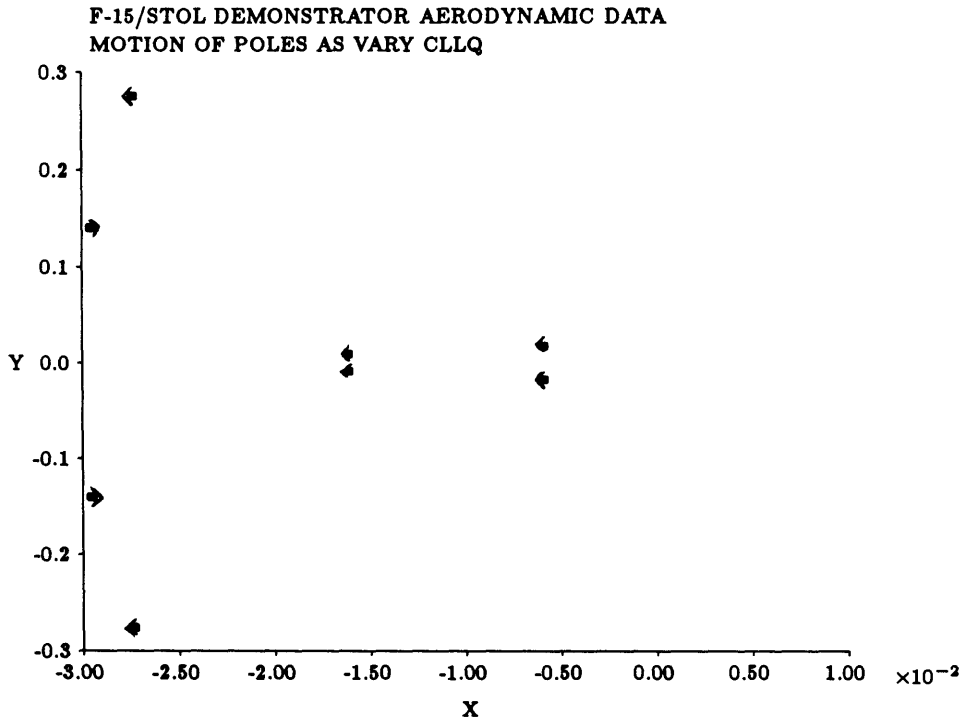

Figure 3.7: Root migration $C_{m_r} = 1$ and C_{l_q} = -1 to 1

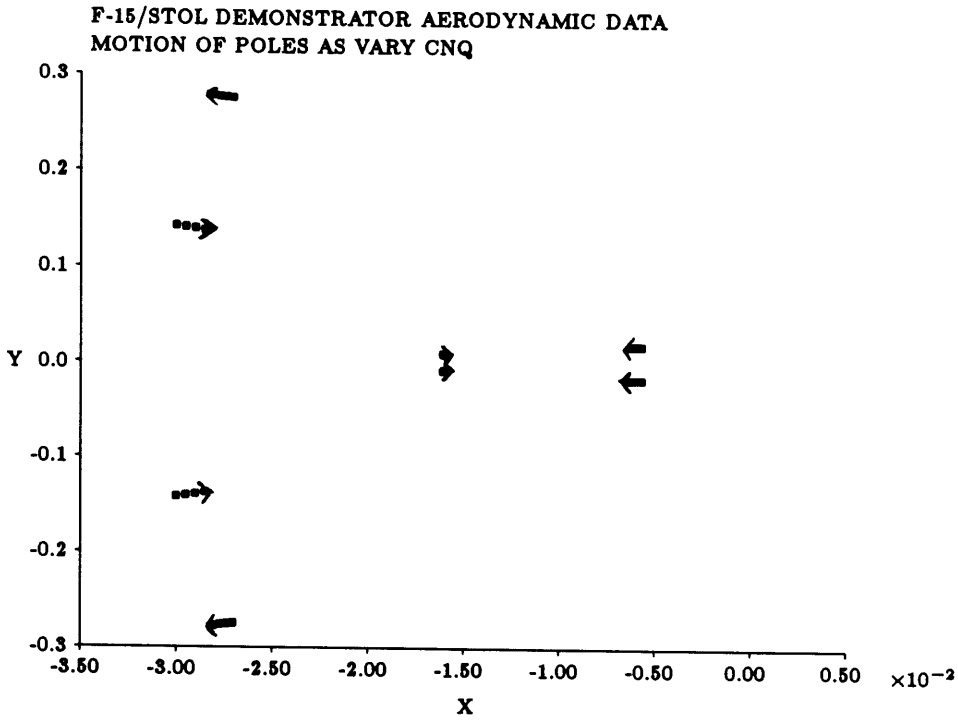

Figure 3.8: Root migration $C_{m_p} = 1$ and C_{n_q} = -1 to 1

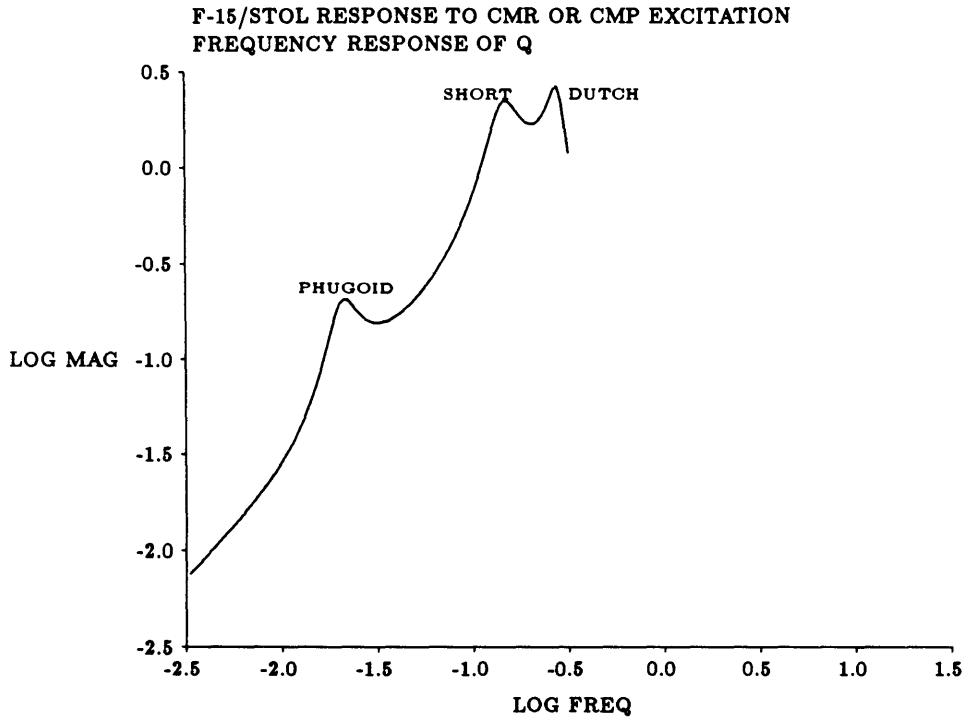

Figure 3.9: Frequency response of q to a C_{m_p} excitation at the dutch roll frequency.

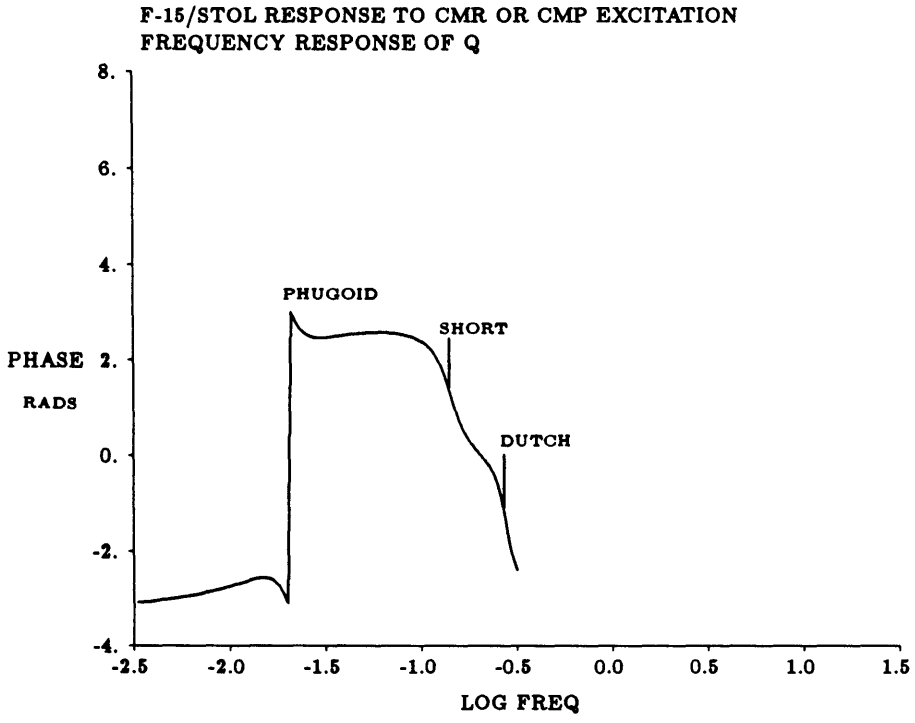

Figure 3.10: Phase of q response to a C_{m_p} excitation at the dutch roll frequency.

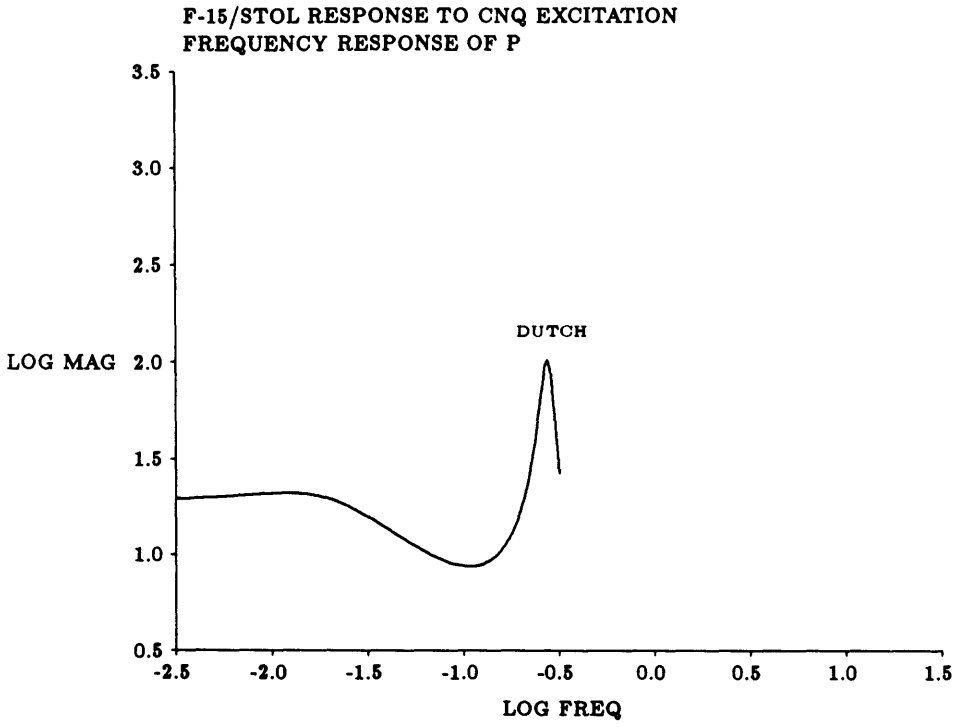

Figure 3.11: Response of p to excitation through C_{n_q}.

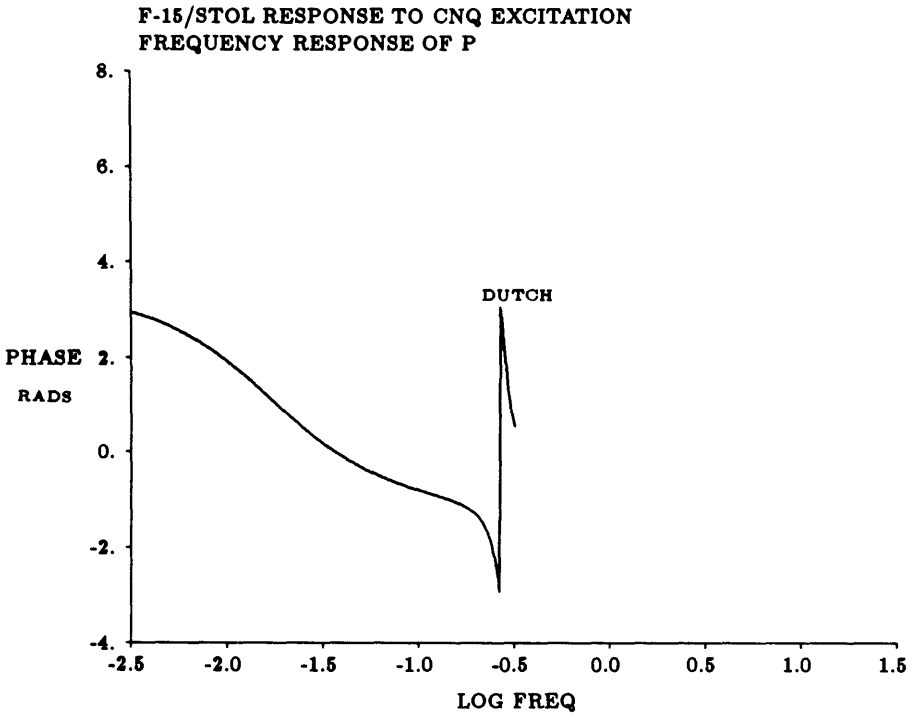

Figure 3.12: Phase of p to excitation through C_{n_q}.

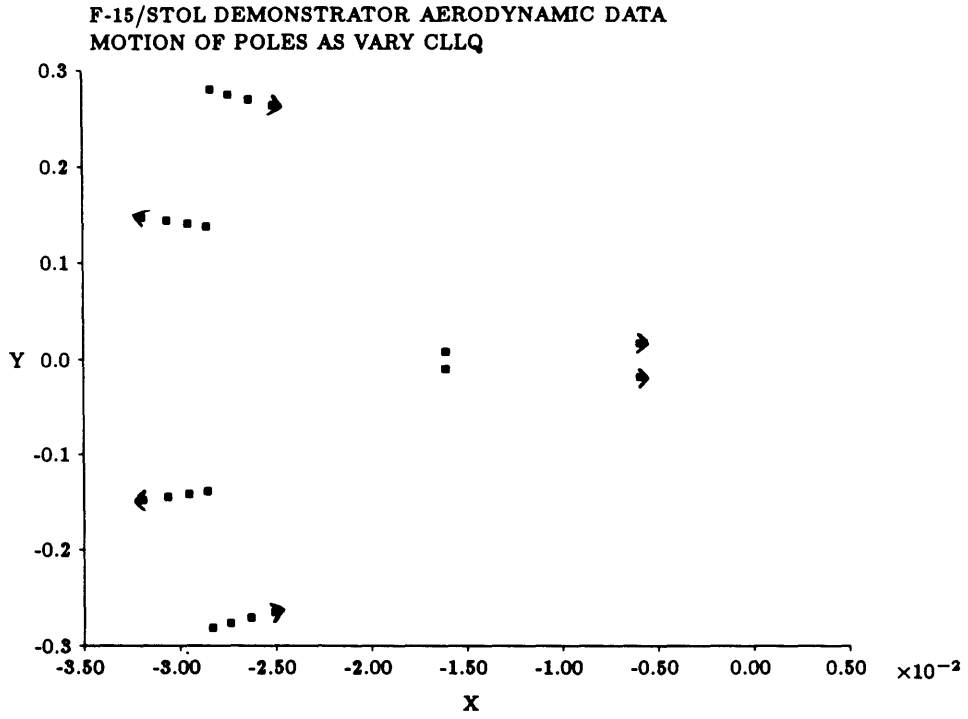

Figure 3.13: Root migration $C_{m_p} = 1$ and C_{l_q} = -1 to 1

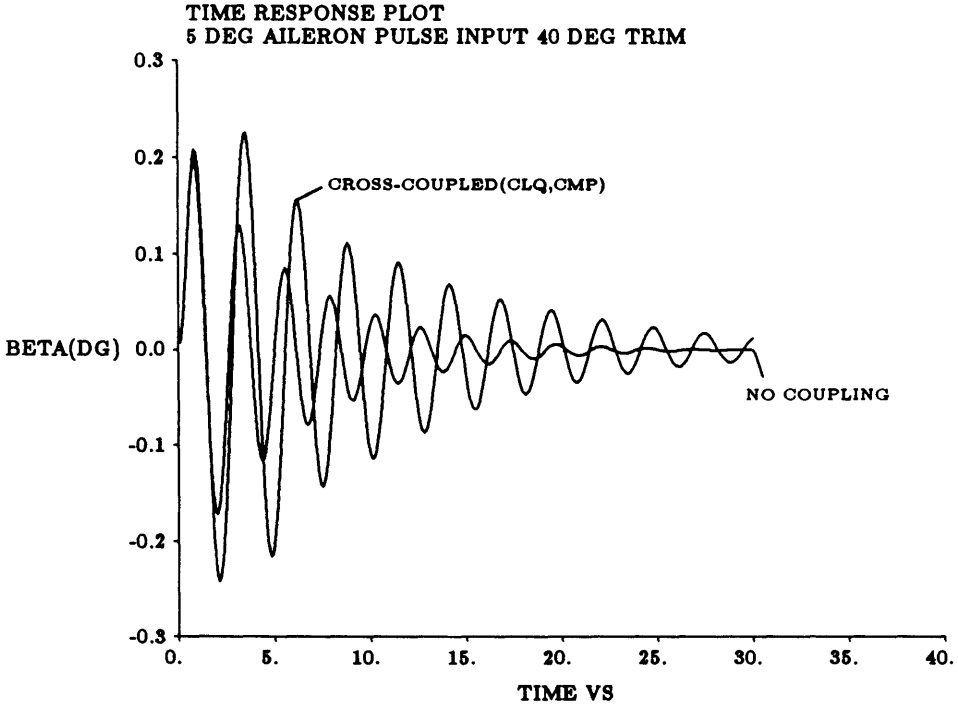

Figure 3.14: Time history of β with and without C_{m_p}, C_{l_q} coupling

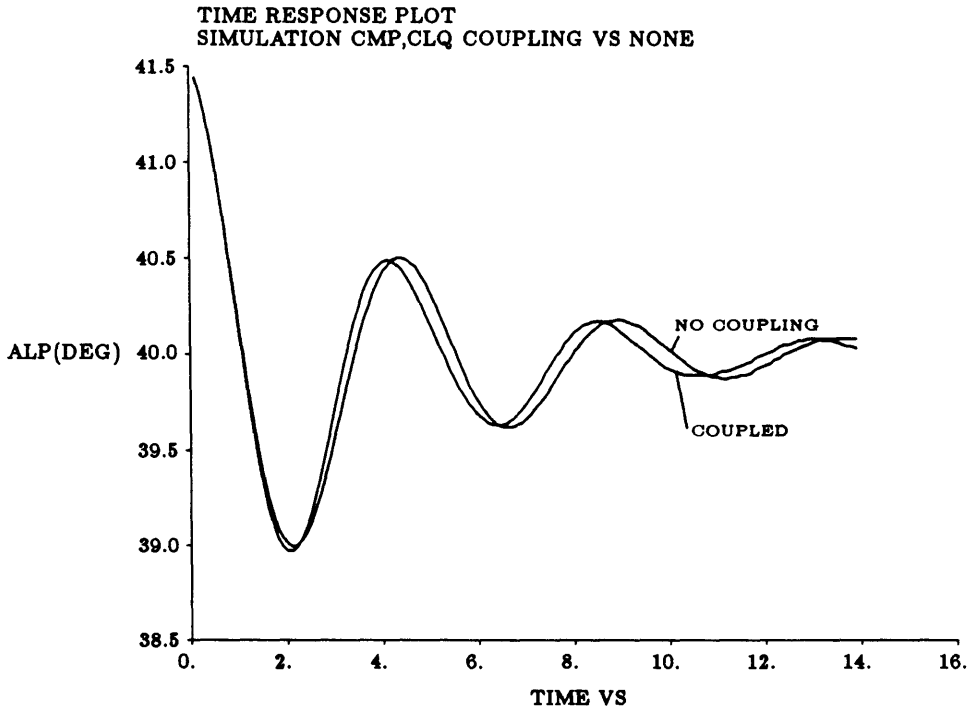

Figure 3.15: Time history of α with and without C_{m_p}, C_{l_q} coupling

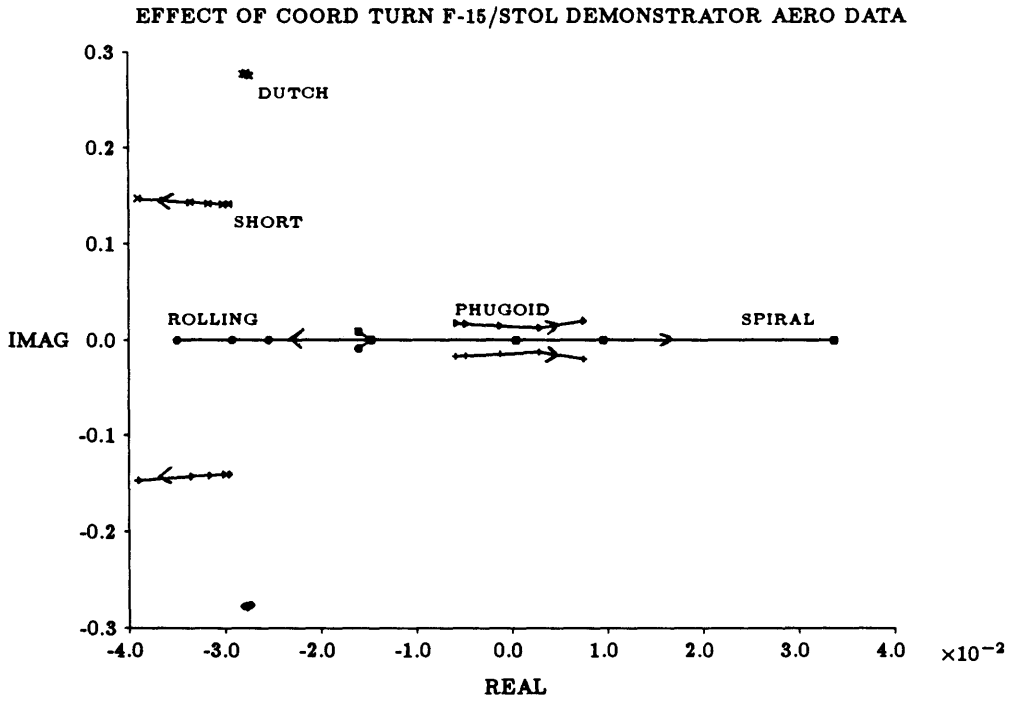

Figure 3.16: Root migration for coordinated turns with rotation rates of 0.05,0.1, 0.15 and 0.2 rad/sec.

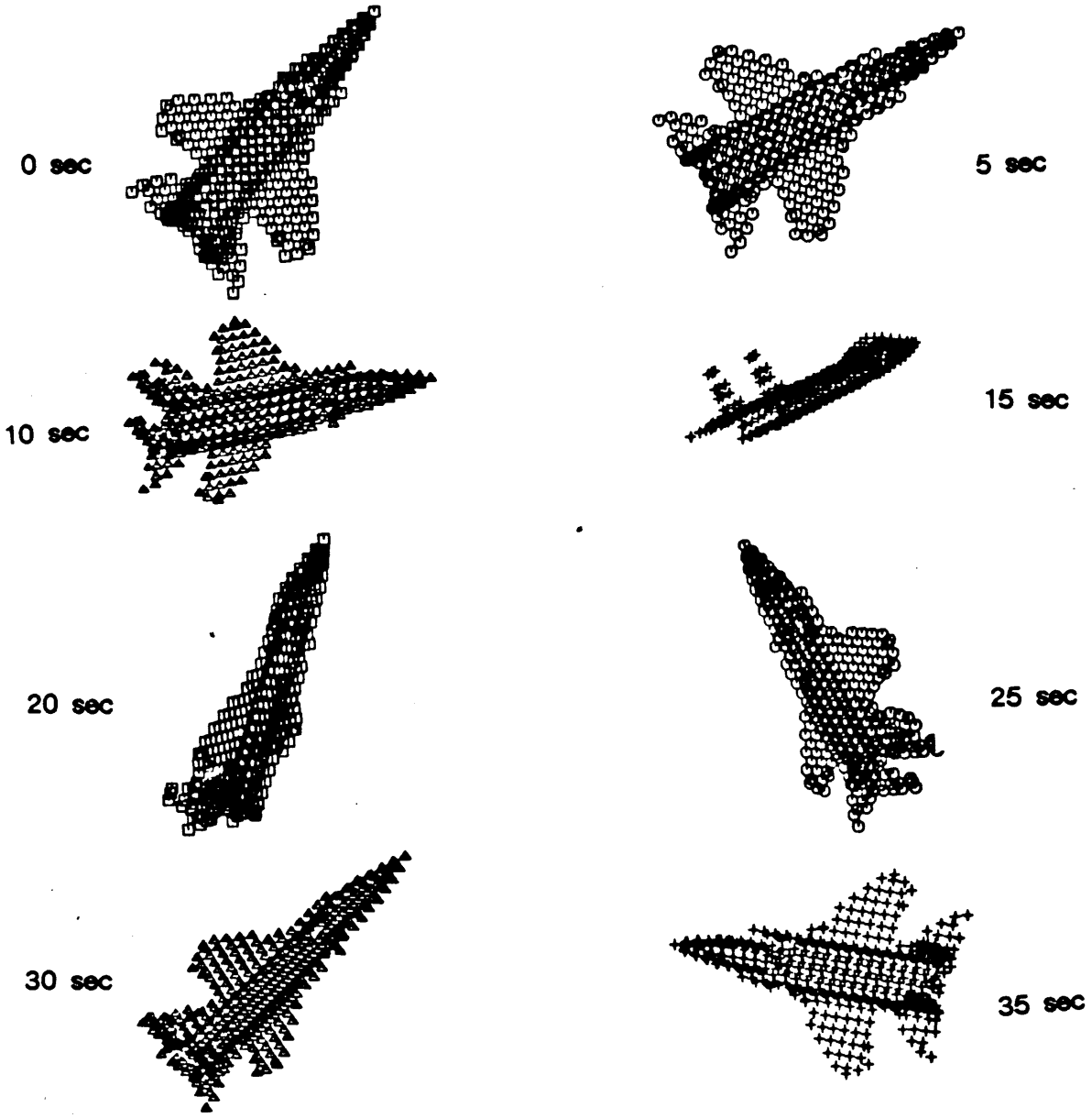

Figure 3.17: Side view at 5 sec intervals of high angle of attack phugoid during a turn.

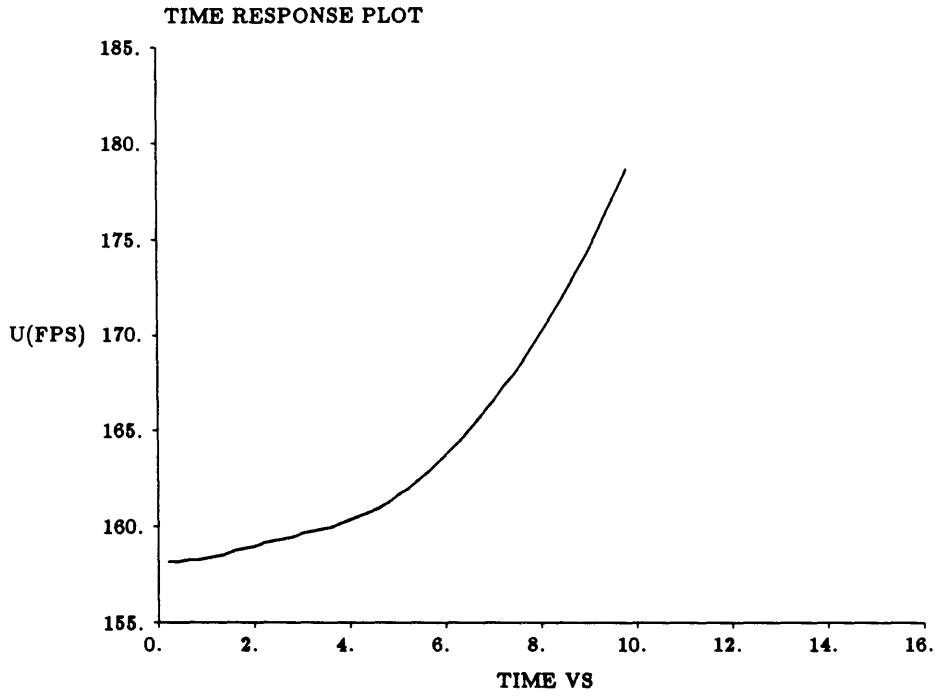

Figure 3.18: Growth of x-velocity at phi=74 deg and alpha=40 deg.

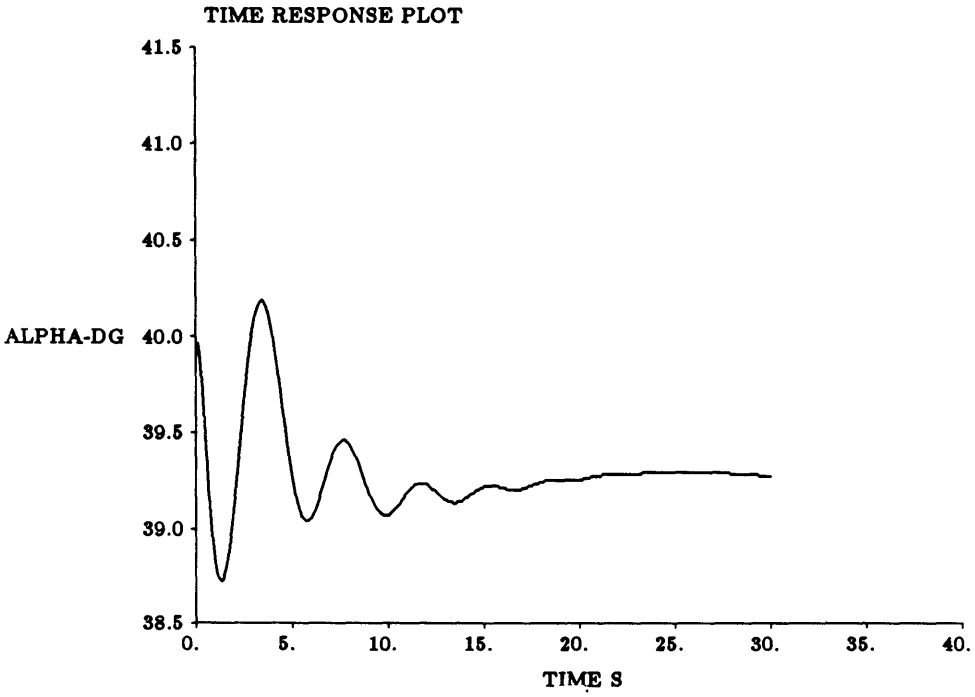

Figure 3.19: Angle of attack variation in turn after 5 deg elevator pulse.

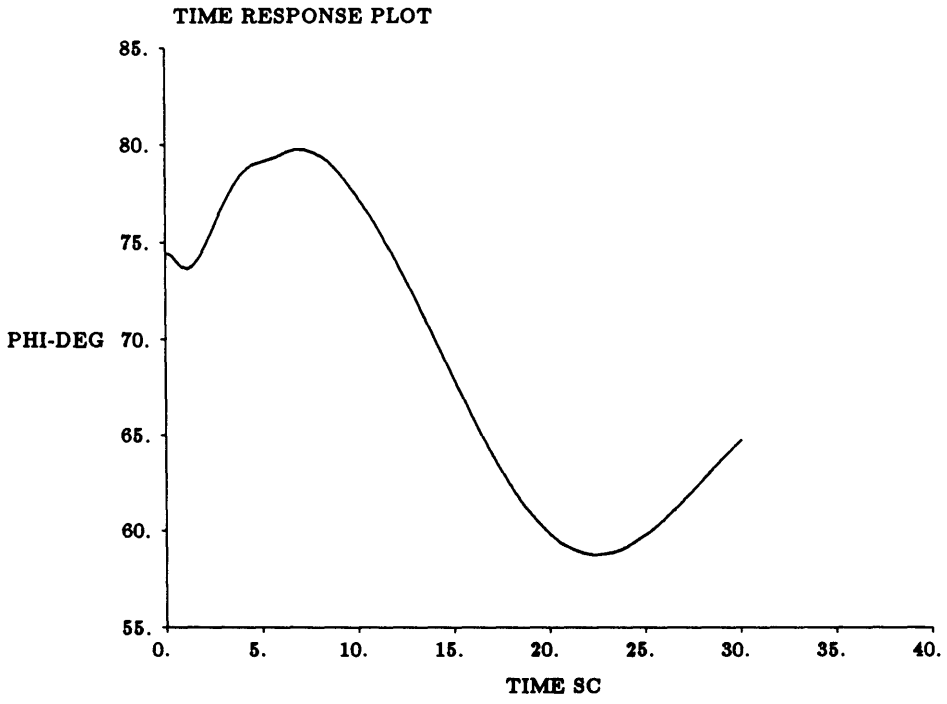

Figure 3.20: Bank angle variation in turn after 5 deg elevator pulse.

Chapter 4
Aerodynamic Lag

Given that our aerodynamic model in the simulator is a frozen point aerodynamic model, it does not include any effects dependent on the history of motion. One of these effects is that of aerodynamic lag. We investigated the effects on aircraft dynamics by including a simple aerodynamic lag model in the longitudinal plane accounting for the time taken for the wing and horizontal tail to develop an aerodynamic force.

4.1 Lag Model

When an airfoil experiences a sudden increase in angle of attack through some sort of motion, the lift does not instantaneously reach its final value. To satisfy no flow through the airfoil, the airfoil must develop more circulation instantaneously. However, Kelvin's theorem requires that equal and opposite circulation be shed into the wake. The effect of the shed vorticity is to decrease the initial change in angle of attack thereby reducing the initially required circulation. As the shed vorticity convects downstream, the airfoil must slowly increase its bound vorticity as it now shares more of the burden of satisfying the boundary condition (the wake vorticity no longer reduces the angle of attack). Thus, the ensuing lift distribution will in theory jump to some value (half of final value) and slowly increase to its final value.

One can determine an airfoil's response to a unit step change in angle of attack (indicial response function) either through messy integral equations or experiments.

Assuming a linear response to changes in angles of attack, the change in lift developing from an arbitrary airfoil motion is the superposition of the lift arising from many small steps in angle of attack. If we call $\phi(t)$ the indicial response of an airfoil, we may use Duhamel's integral to write the ensuing lift coefficient as:

$$C_L(t) = \int_0^t \phi(t-\tau)\frac{dC_L(\tau)}{dt}d\tau \tag{4.1}$$

We can use the lift curve slope (C_{L_α}) to rewrite the above as:

$$C_L(t) = C_{L_\alpha}\int_0^t \phi(t-\tau)\dot{\alpha}(\tau)d\tau \tag{4.2}$$

Alternatively, we can consider an effective angle of attack given by:

$$\alpha_{eff}(t) = \int_0^t \phi(t-\tau)\dot{\alpha}(\tau)d\tau \tag{4.3}$$

Since the simulator data is a lookup table, we used the above angle of attack to lookup the wing's lift and pitching moment coefficients. To minimize time computing, we integrated only over the previous 100 time steps. Our computer model sum was:

$$\alpha_{eff-wing}(nT) = \sum_{j=(n-100)T}^{nT} \phi(nT-j)(\alpha(j)-\alpha(j-1)) \tag{4.4}$$

Where T is the iteration time step and n is the iteration number. The specific indicial response function used was (from Venkatesan and Friedmann, 1986):

$$\phi(\tau) = 1 - .203e^{-.072\tau} - .236e^{-.261\tau} - .06e^{-.8\tau} \tag{4.5}$$

where τ is a non-dimensionalized time defined as:

$$\tau = \frac{2(VT)}{\bar{c}}t \tag{4.6}$$

In addition to the wing, the tail will also have an aerodynamic lag associated with it. While its effect may not be important in the lift, it will be significant in the pitching moment. Two effects are worth noting:

- The tail has an indicial response function as above except that the non-dimensional time is based on the tail chord length.
- The downwash on the tail stems from vortices shed off the wing at some earlier time (these vortices convect to the tail in time=$\frac{l_t}{VT}$).

The small size of the tail's chord makes the first effect smaller than the second (faster indicial response). However, the aerodynamic model for the simulator uses fixed point force coefficients based on the aircraft angle of attack. Thus, to include the effect of the tail, we must compute an effective angle of attack for the aircraft. This effective angle corresponds to the aircraft angle of attack that yields the desired tail angle of attack under steady state conditions.

Under steady state the angle of attack felt by the tail is given by:

$$\alpha_t = \alpha_w - \frac{d\epsilon}{d\alpha_w}\alpha_w + i_t \tag{4.7}$$

where ϵ is the downwash angle at the tail and i_t is the incidence angle of the tail. As the aircraft maneuvers, the tail will feel the downwash from the wing a small time earlier due to the delay in the wing vortices advecting to the tail. Combining this with the fact that the downwash variation with angle of attack is about one-half yields:

$$\alpha_t(t) = \alpha_{actual}(t) - \frac{1}{2}\alpha_w(t - \frac{l_t}{VT}) \tag{4.8}$$

We have assumed no incidence angle. Under steady state conditions however, our aircraft angle of attack and wing angle of attack are related through:

$$\alpha_w = 2\alpha_t \tag{4.9}$$

Thus to get the proper tail angle of attack, we had to input an aircraft angle of attack given by:

$$\alpha_{AC-tail}(t) = 2\alpha_{actual}(t) - \alpha_w(t - \frac{l_t}{VT}) \tag{4.10}$$

Another aspect of our model that deserves attention is the fact that our simulation did not break down the loads due to different components. Thus, we had to divide the lift and pitching moments into fractions due to the various aircraft components. Our lag was only present in the following terms:

- Basic lift coefficient (93% wing, 7% tail).
- Basic pitching moment coefficient (90% tail, 10% wing).
- Pitching moment due to elevator (100% tail).
- Pitching moment due to pitch rate (100% tail).

For instance, our basic lift coefficient was given by:

$$C_{L_0} = 0.93 C_L(\alpha_{eff-wing}) + 0.07 C_L(\alpha_{AC-tail}) \tag{4.11}$$

We included the above model into our simulator and ran some cases at high and low Mach number (0.6 and 0.2). However, at the higher mach number the lag had only a small effect.

4.2 Effect of Wing Lag at Low Speed

When we ran the simulation with only the wing lag model (no tail lag) which would correspond to a delta wing aircraft, we get the angle of attack response shown in figure 4.1. Our disturbance is an initial step in angle of attack from straight and level. Comparing the response with the lag model, we see that the effect of the wing lag decreases the damping and increases the period of oscillation. The half-time increases from 2.3 seconds to 4.9 seconds whilst the period increases from 4.6 seconds to 4.75 seconds.

We included the lag model into the linearized longitudinal equations to predict the motion of the longitudinal roots with the lag model included. We note that the Laplace transform of the indicial response function is given by:

$$\phi(s) = \frac{0.5s^3 + .69185s^2 + .22808s + .01503}{s(s+.72)(s+.261)(s+.8)} \tag{4.12}$$

Noting that our angle of attack is the convolution of the indicial response function with the time derivative of angle of attack gives us the following Laplace transform of the wing angle of attack:

$$\alpha_{eff-wing}(s) = s\phi(s)\alpha_{actual}(s) \tag{4.13}$$

Where our actual angle of attack is the disturbance angle of attack from straight and level. This angle is used to compute the basic lift and pitching moment coefficients as well as pitching moment due to aileron and pitching moment due to pitch rate. Since the angle of attack dependency of the pitching moment due to pitch rate enters non-linearly, we do not include this effect in our linearized model. We first consider the pitching moment as given by:

$$C_m = C_{m_0}(\alpha_{trim}) + \frac{dC_{m_0}}{d\alpha}\alpha_{eff-wing} + C_{m_{\delta H}}(\alpha_{trim})\delta H_{trim} + \frac{dC_{m_{\delta H}}}{d\alpha}\alpha_{eff-wing}\delta H_{trim} \tag{4.14}$$

Thus, our C_{m_α} term in our linearized pitching moment equation (see Equation 1.3) is replaced by:

$$\frac{dC_{m_0}}{d\alpha}s\phi(s) + \frac{dC_{m_{\delta H}}}{d\alpha}s\phi(s)\delta H_{trim} \tag{4.15}$$

Similarly, we may write the basic lift coefficient as:

$$C_{L_0} = C_{L_0}(\alpha_{trim}) + \frac{dC_{L_0}}{d\alpha}\alpha_{eff-wing} \tag{4.16}$$

This gives us:

$$C_{L_\alpha}(s) = \frac{dC_{L_0}}{d\alpha}s\phi(s) \tag{4.17}$$

	Linear Roots		Simulator	
Mode	Period(sec)	Half-time	Period(sec)	Half-Time
Short (no lag)	4.63	2.43	4.6	2.3
Short (lag)	4.7	4.8	4.8	4.9

Table 4.1: Period and Half-times with and without wing lag for simulator and linear model.

We must then use the fact that:

$$C_x = C_L \sin\alpha - C_D \cos\alpha + \frac{T}{\bar{q}S} \tag{4.18}$$

and:

$$C_Z = -C_D \sin\alpha - C_L \cos\alpha \tag{4.19}$$

to relate the C_{L_α} term to C_{x_α} and C_{Z_α} by taking simple derivatives.

Inclusion of this lag model into our longitudinal equations of motion gives us the roots shown in figure 4.2 (note that we now non-dimensionalized using the wing chord, not the span). The phugoid roots are not moved by our lag model. The short period's damping is 51% of its previous (no lag) value. The damped natural frequency is decreased by 2.3% . This gives us the same results as our simulation. The effects on the short period are summarized in Table 4.1 . Other poles appear due to the lag, but these are close to the zeroes stemming from the lag.

A physical explanation for the short period reduction in damping is that a change in angle of attack will not yield as large a change in both lift coefficient and pitching moment coefficient as without the lag. Thus, the C_{L_α} and C_{m_α} magnitudes appear to suffer a reduction. Since these terms classically affect the short period damping, the damping is reduced by the lag model.

	Linear Roots		Simulator	
Mode	Period(sec)	Half-time	Period(sec)	Half-Time
Short (no lag)	4.63	2.43	4.6	2.3
Short (lag)	4.5	1.9	4.4	1.8

Table 4.2: Period and Half-times with and without total lag for simulator and linear model.

4.3 Effect of Wing and Tail Lag at Low Speed

We then included the full lag model in the simulation to see the effect of the tail lag on the short period. The same disturbance as before yields the response in angle of attack shown in figure 4.3. By comparing the response with the full lag model, we can see that the effect of the lag is to increase the damping and slightly increase the frequency.

As before, we attempt to predict the effect on the roots by solving for the linearized longitudinal equations. The Laplace transform of the aircraft angle of attack for tail variables gives us:

$$\alpha_{AC-tail}(s) = (2 - e^{-\frac{l_t}{VT}s}s\phi(s))\alpha(s) \tag{4.20}$$

$$\approx \left(2 - s\phi(s)(1 - \frac{l_t}{VT}s)\right)\alpha(s) \tag{4.21}$$

We may then use the above value of $\alpha_{AC-tail}$ instead of α in the appropriate terms (ie. 90% of C_{m_α}, etc.) of the linearized longitudinal equations. Solving for the roots of these equations, we get those shown in figure 4.4. The linearized model predicts the increased short period damping and frequency observed by simulation and no phugoid motion. Once again, the poles stemming directly from our lag model are very close to the zeroes from the lag model.

A comparison of the different short periods is given in Table 4.2. We get close agreement between simulation and linearized roots.

As the aircraft experiences a sudden change in angle of attack, the wing's lift does not develop immediately. Moreover, the tail will not experience the downwash from the wing until the wing vortices convect to the tail (time=$\frac{l_t}{V_T}$). The effect is that the tail immediately experiences the full change in angle of attack without the ensuing downwash. The tail will hence produce more restoring moment with the lag model than without. We can consider this as an increase in magnitude of the effective C_{m_α} which tends to increase the damping.

In comparing the wing lag model to the full lag model (wing and tail), the damping will either increase or decrease depending on the relative importance of the wing lag or tail lag. Thus a delta wing aircraft without horizontal tail will have less damping due to the wing's lag. A conventional aircraft will have competing effects between the wing and tail (the tail will cause an increase in damping whilst the wing will force a decrease in damping).

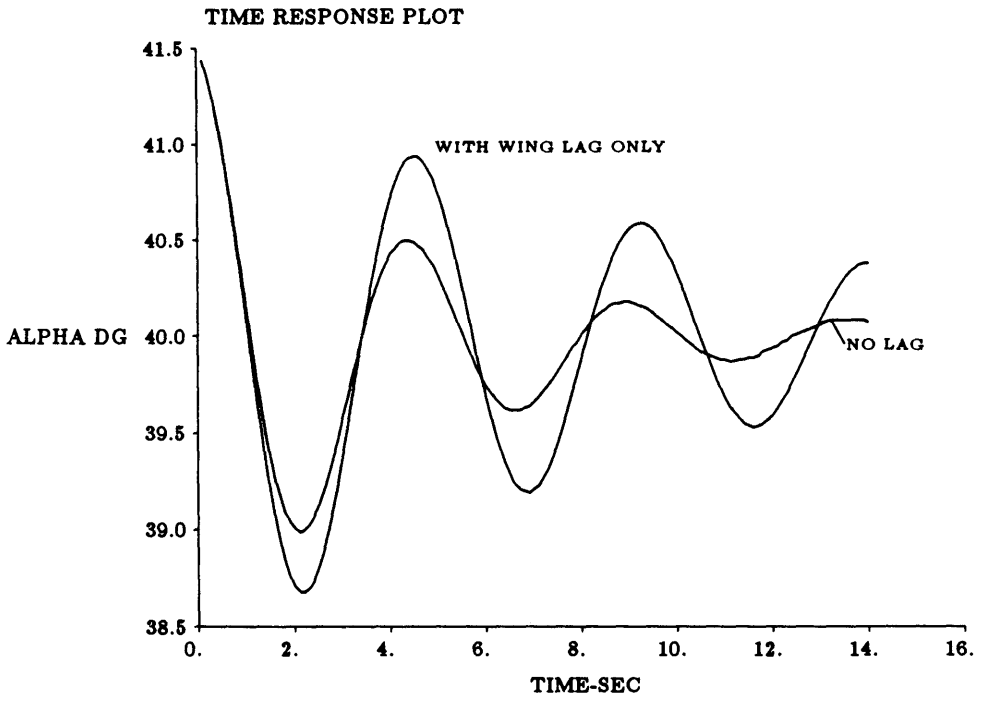

Figure 4.1: Response in AOA with and without wing lag model for AOA disturbance.

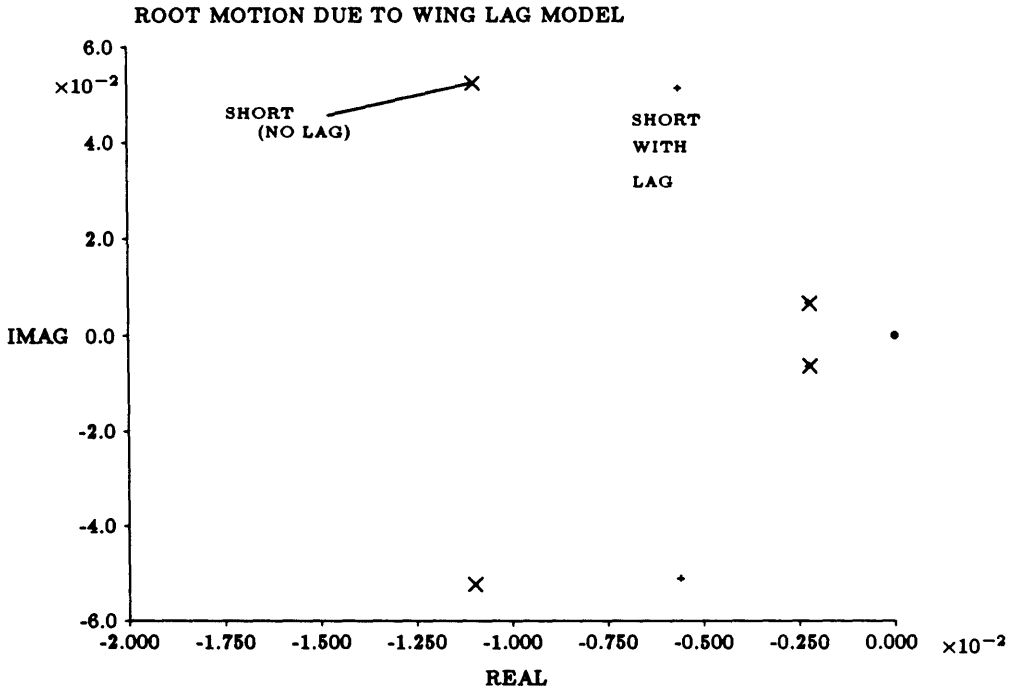

Figure 4.2: Dominant roots of wing lag model compared with roots without lag.

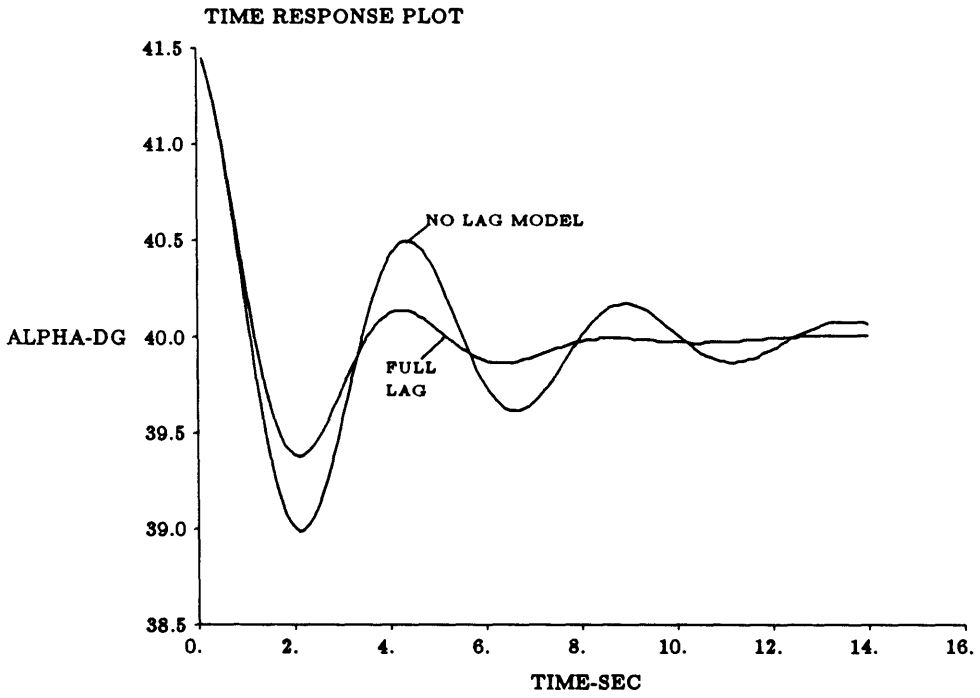

Figure 4.3: Response in AOA with and without full lag model for AOA disturbance.

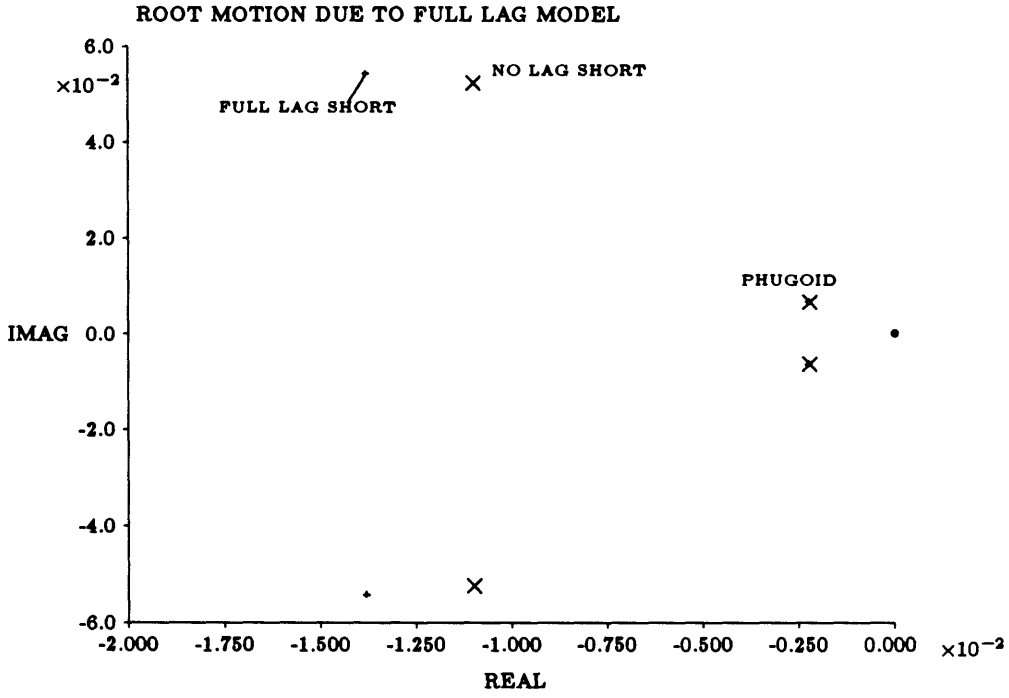

Figure 4.4: Dominant roots of full lag model compared with roots without lag.

Chapter 5
Nonlinearities

Previously, we have assumed that the high angle of attack equations of motion behave in an essentially linear fashion. While this might be approximately true for small pertubations about the point of linearizaion, the dynamical equations and their corresponding aerodynamic terms are decidedly nonlinear. As the aircraft enters the high angle of attack domain, the aerodynamic nonlinearities get stronger and the corresponding linear 'small' pertubation region decreases. This is particularly true for the case of discontinuities in the loads due to sudden flow separation or vortex bursting. Some other strong aerodynamic nonlinearities that develop are:

- Strong dependency of all classical stability derivatives on angles of attack and sideslip.
- Rate dependency of the moments due to rotation.
- Large hysterisis loops in the load coefficients.
- Sudden peaks in moments.

We looked at some of the above aerodynamic nonlinearities to see what their effects were on the aircraft dynamics.

5.1 Quadratic Pitching Moment

To see the effects of a slightly nonlinear pitching moment dependency on angle of attack, we modelled a pitching moment coefficient which was quadratically dependent on angle of attack. Figure 5.1 shows a comparison of the simulator data pitching moment coefficient versus our curve fitted data.

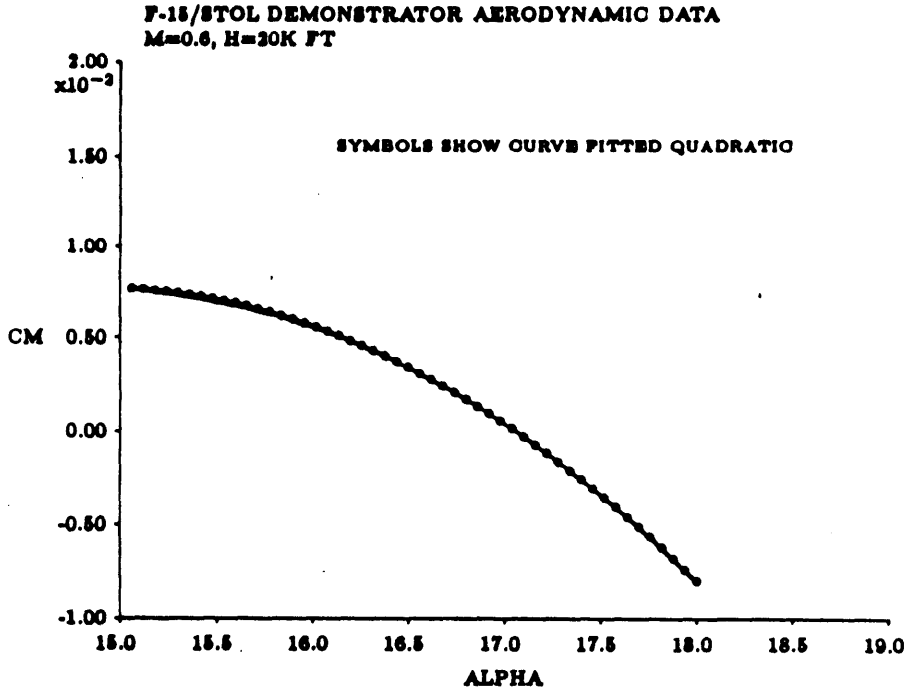

Figure 5.1: Comparison of actual Pitching moment coefficient to quadratic fit.

With the squared pitching moment, our constant speed longitudinal equation becomes:

$$I_{yy}\ddot{\alpha} - \left(I_{yy}\frac{Z_\alpha}{mu_0} + \bar{q}S\bar{c}C_{m_q}\right) alpha - \bar{q}S\bar{c}C_{m_\alpha}(1+\epsilon\alpha)\alpha = \bar{q}S\bar{c}C_{m_{\delta_e}}\delta_e \qquad (5.1)$$

Where ϵ is the coefficient of the quadratic term in the pitching moment.

We can solve for the above homogenous equation using regular pertubations methods

to first order in ϵ. This yields:

$$\alpha = e^{-\varsigma\omega_n t}(C\cos\omega_d t + D\sin\omega_d t) + \epsilon e^{-\varsigma\omega_n t}(F + A\cos 2\omega_d t + B\sin\omega_d t) \tag{5.2}$$

$$\omega_n = \sqrt{-\frac{\bar{q}S\bar{c}C_{m_\alpha}}{I_{yy}}} \tag{5.3}$$

$$\varsigma\omega_n = 0.5\left(\frac{Z_\alpha}{mu_0} + \frac{\bar{q}S\bar{c}C_{m_q}}{I_{yy}}\right) \tag{5.4}$$

We can relate the coefficients of the higher order terms to the lower order ones as follows:

$$F = -.5\left(C^2 + D^2\right) \tag{5.5}$$

$$A = \frac{(4\varsigma\sqrt{1-\varsigma^2})(4\varsigma^2-3)}{(4\varsigma^2-3)^2 + 16\varsigma^2(1-\varsigma^2)}\left(\frac{D^2-C^2}{8\varsigma\sqrt{1-\varsigma^2}} - \frac{CD}{8\varsigma^3-6}\right) \tag{5.6}$$

$$A = \frac{(4\varsigma\sqrt{1-\varsigma^2})(4\varsigma^2-3)}{(4\varsigma^2-3)^2 + 16\varsigma^2(1-\varsigma^2)}\left(\frac{C^2-D^2}{8\varsigma^3-6} - \frac{CD}{8\varsigma\sqrt{1-\varsigma^2}}\right) \tag{5.7}$$

$$\tag{5.8}$$

When we compare the above solution to the one with ϵ set to zero, we get much closer to the simulation with our quadratic model. Figure 5.2 compares the above quadratic solution to the simulation whilst figure 5.3 compares the linear model to the simulator result. The case run in the simulation is that of an elevator doublet response about a trim angle of attack of 17.06 degrees at Mach .6 .

5.2 BTS Approach

A more general approach to get the effect of slight nonlinearities on aircraft dynamical response was investigated. We tried to modify the BTS method (see Christopher and Thorne 1985 for a broader treatment) to include even powers of nonlinear terms.

We begin with an autonomous nonlinear system given by:

$$\dot{x} = Ax + f(x) \tag{5.9}$$

where x, $\dot{x}$ and $f(x)$ are n-sized vectors and $f(x)$ represents the nonlinear terms in x. The BTS method assumes a solution of the form (where ξ and η are n-sized vectors):

$$x = a(t)\{\xi(t)\sin\phi(t) + \eta(t)\cos\phi(t)\} \tag{5.10}$$

By then substituting into the original equation (Eqn 5.9), and subsequently multiplying by both $\sin\phi$ and $\cos\phi$ and integrating over one period of ϕ, one can get two time averaged vector equations. A further simplification is made by assuming that derivatives with respect to a are zero. The problem with this method is that it cannot solve for nonlinearities which are even powers of x (ie. x_1^2 or x_1x_2 etc.) because these nonlinear terms will always vanish in the averaging process. To try to correct for this deficiency, and given our preceeding solution for a quadratic pitching moment, we started with the following assumption:

$$x = a(t)\{\xi_1(t)\sin\phi(t) + \eta_1(t)\cos\phi(t)\xi_2(t)\sin 2\phi(t) + \eta_2(t)\cos 2\phi(t)\} \tag{5.11}$$

By substituting the above result into our original equations and averaging as before, we get two vector equations. Additional equations are arrived at by multiplying by $\cos 2\phi$ or $\sin 2\phi$ and averaging.

We used the above method (modified and not modified) to predict the effect on the following test equation (chosen for simplicity):

$$\dot{x_1} = x_2 \tag{5.12}$$

$$\dot{x_2} = c_1x_1 + c_2x_2 + c_3x_1^2 + c_4x_1^3 \tag{5.13}$$

We solved for the above equations using a four step Runge-Kutta scheme and compared this solution to the linear system's and to the BTS model's solution. We ran three cases:

- A cubic nonlinearity ($c_1 = -1$,$c_2 = -.5$,$c_3 = 0$, and $c_4 = -1$).
- A squared nonlinearity ($c_1 = -1$,$c_2 = -.5$,$c_3 = -.5$, and $c_4 = 0$.).

- Both nonlinearities ($c_1 = -1, c_2 = -.5, c_3 = -.5$, and $c_4 = -1$).

In the first case, the BTS method proved to be a significant improvement over the linear model (we knew this from Christopher and Thorne, 1985) as is shown in figure 5.4. Our modified BTS method was still not capable of capturing the effect of the squared nonlinearity as is shown in figure 5.5. The rms error in x_1 for the various cases is given below:

Model	Cubic	Squared	Both
Linear	.0128	.0090	.0192
BTS+	.0020	.0083	.0073

It is clear that the above procedure is not the correct approach to predict the effect of squared nonlinearities. Perhaps a relaxation of the condition that the derivatives with respect to $a(t)$ be zero is necessary since our solution procedure does not yield the proper amplitude oscillation.

5.3 Effect of Discontinuities

We know that the aerodynamic forces and moments can contain significant jumps due to stall and vortex bursting. We included such a model for stall in the simulator by modifying the lift and pitching moment curves to look like figure 5.6. The variation in moment was chosen to resemble that of an airfoil undergoing dynamic stall (see NASA TM 81264). The effect of this model is to produce a limit cycle in angle of attack and pitch (see figure 5.7 and figure 5.8). Each time the aircraft reaches the stall angle of attack, the sudden strong forcing in pitching moment and Z-force cause a large change in $\dot{\alpha}$. The limit cycle develops at the point where the damping in one cycle (gradual) matches the forcing due to the discontinuities.

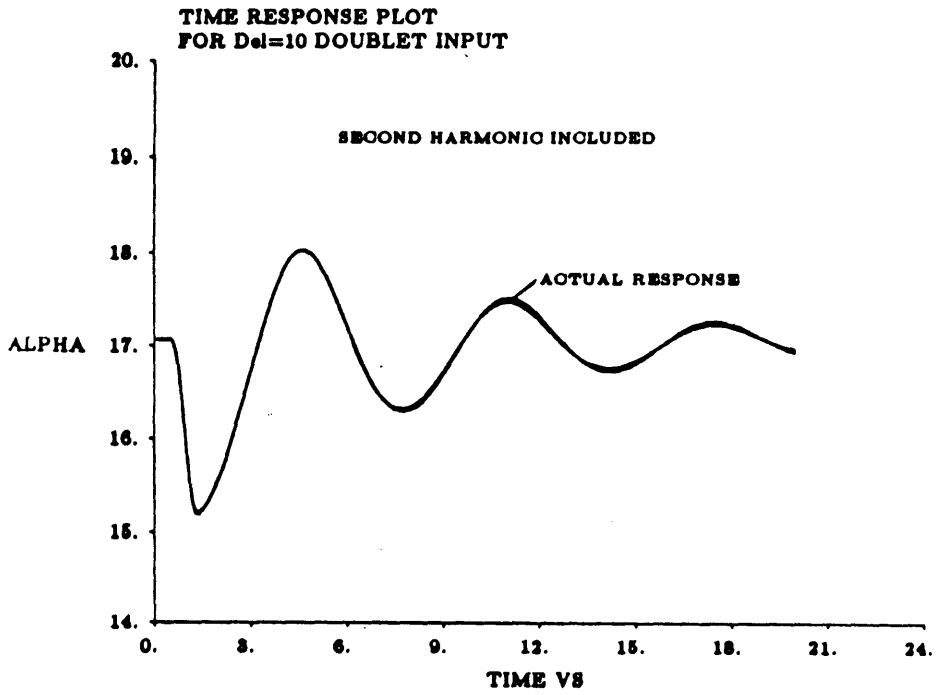

Figure 5.2: Comparison of doublet response to solution with second harmonics.

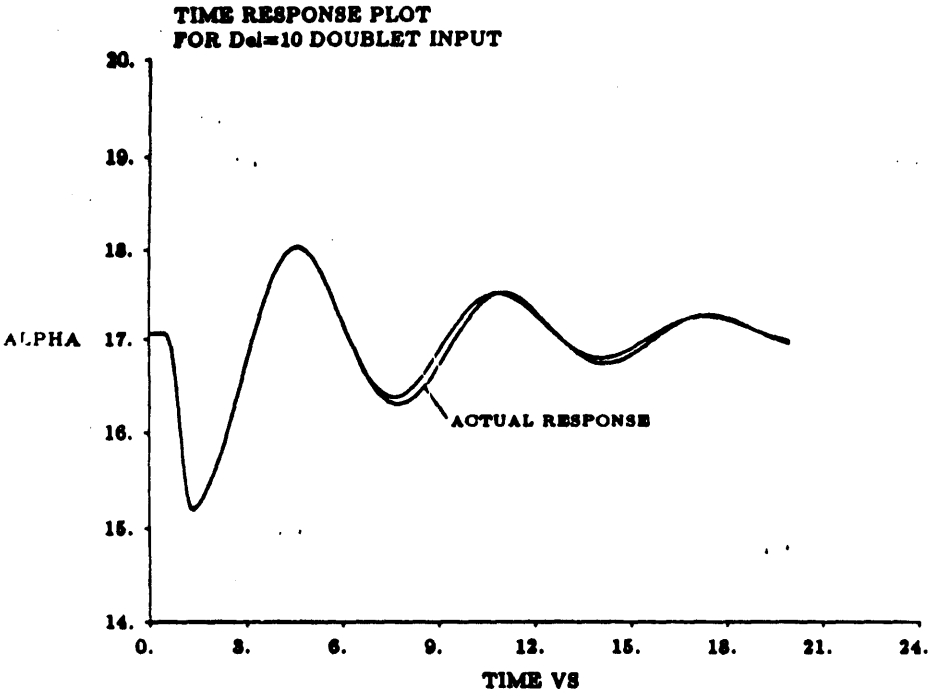

Figure 5.3: Comparison of doublet response to linear solution.

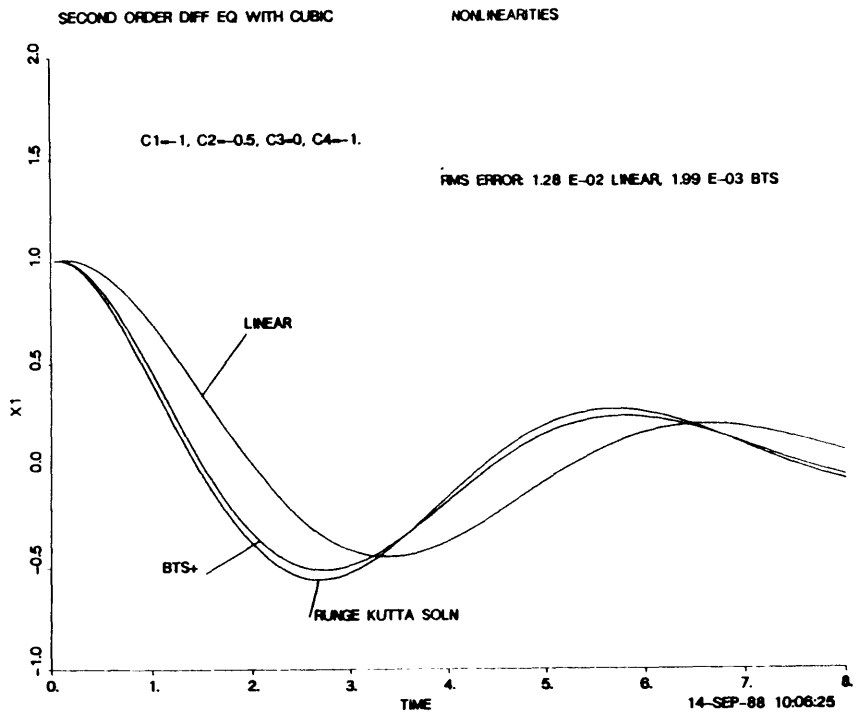

Figure 5.4: Cubic nonlinearity solution compared to BTS method and linear model.

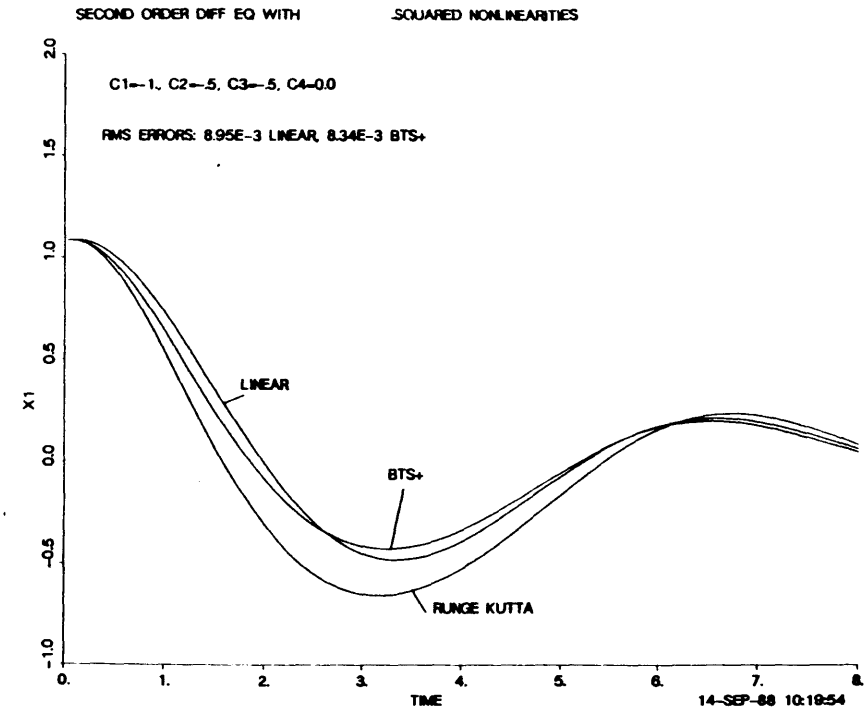

Figure 5.5: Squared nonlinearity solution compared to BTS method and linear model.

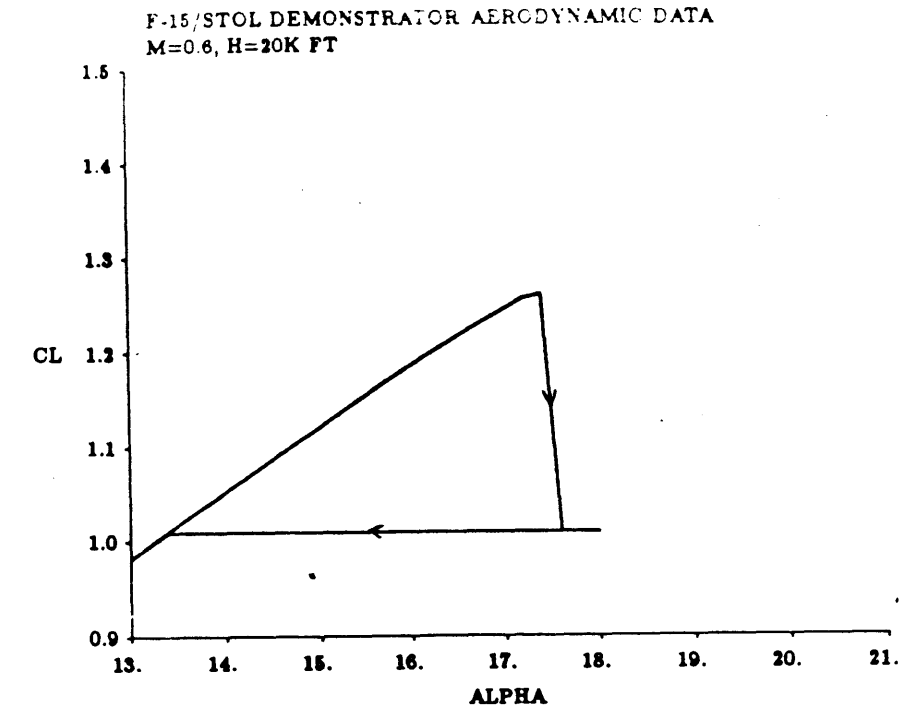

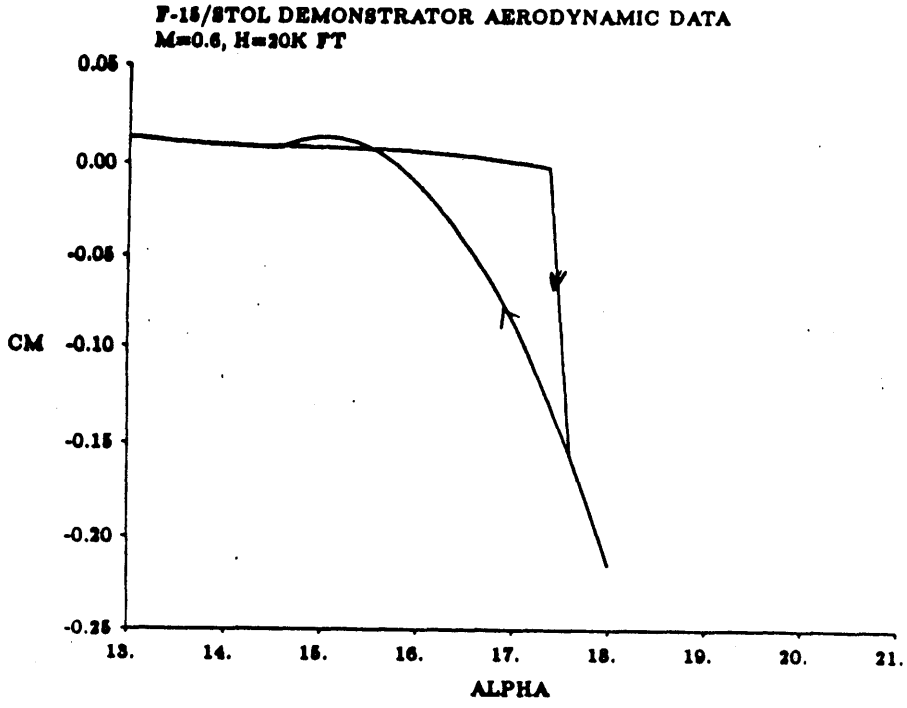

Figure 5.6: Lift and pitching moment curves for stall hysterisis model.

5.3.1 Discontinuity in sideforce coefficient

At a trim angle of attack of 40 degrees, the wind tunnel aerodynamic data gave us a discontinuity in sideforce when the sideslip became positive. This sideforce coefficient is shown as a function of sideslip angle in figure 5.9. This term also leads to a limit cycle oscillation (albeit small in amplitude) in the sideslip. This limit cycle is shown for the sideslip phase plane and time response in figures 5.10 and 5.11. If we assume a damped sinusoidal solution for sideslip (ie. at the dutch roll root), the limit cycle is that for which the jump in sideforce exactly offsets the damping in half a period. Clearly any less damping yields a solution that grows to the limit cycle and any more damping gives us a solution that decays to the limit cycle.

Although the above limit cycle was small in magnitude, clearly its magnitude can increase as the discontinuity becomes larger.

5.4 Short Time Scale Motion

The mechanism through which the various aircraft control surfaces act is by forcing moments which then integrate through the equations of motion to give rise to changes in aircraft attitude (Euler) angles and velocities. Thus, the initial (short time scale) response to a control input will be given by the rotation equations. In addition, the translational equations will feedback information to the rotation equations only through: the pitching moment due to angle of attack (C_{m_α}), the rolling moment due to sideslip (C_{l_β}), and the yawing moment due to sideslip (C_{n_β}). Thus, the rotation equations will also decouple if these parameters become very small.

The rotational equations are repeated below for convenience:

$$\dot{p} = \frac{-\left(\frac{I_x - I_y}{I_x} + \frac{I_{xz}^2}{I_x I_z}\right) qr + \left(1 - \frac{I_y - I_z}{I_x}\right) \frac{I_{xz}}{I_x} pq + \frac{\bar{q}Sb}{I_x}\left(C_l + \frac{I_{xz}}{I_x} C_n\right)}{1 - \frac{I_{xz}^2}{I_x I_z}} \tag{5.14}$$

$$\dot{q} = \frac{\bar{q}S\bar{c}}{I_y} C_m + \left(\frac{I_z - I_x}{I_y}\right) pr + \frac{I_{xz}}{I_y}(r^2 - p^2) \tag{5.15}$$

$$\dot{r} = \frac{\left(\frac{I_{xz}^2}{I_x I_z} - \frac{I_y - I_z}{I_z}\right) pq - \left(1 + \frac{I_z - I_y}{I_z}\right) \frac{I_{xz}}{I_z} qr + \frac{\bar{q}Sb}{I_z}\left(\frac{I_{xz}}{I_z} C_l + C_n\right)}{1 - \frac{I_{xz}^2}{I_x I_z}} \tag{5.16}$$

If we simply express the moments as due to the various rotation rates and control deflections:

$$C_l = C_{l_{\hat{p}}}\hat{p} + C_{l_{\hat{r}}}\hat{r} + C_{l_{\delta_{rud}}}\delta_{rud} + C_{l_{\delta_{ail}}}\delta_{ail} \tag{5.17}$$

$$C_m = C_{m_{\hat{q}}}\hat{q} + C_{m_{\delta_H}}\delta_H \tag{5.18}$$

$$C_n = C_{n_{\hat{p}}}\hat{p} + C_{n_{\hat{r}}}\hat{r} + C_{n_{\delta_{rud}}}\delta_{rud} + C_{n_{\delta_{ail}}}\delta_{ail} \tag{5.19}$$

and we have $I_{xz} = 0$ as well as $I_y = I_z$ then we get the Lorenz equations with varying coefficients (see Thompson, 1988).

Our knowledge of the Lorenz equations teaches us that for certain values of the coefficients, these equations can yield a chaotic attractor. The major implication of this chaotic attractor is that the solution depends sensitively on initial conditions. Thus, the path of two nearby points in phase space may diverge exponentially. A consolation may be had by realizing that linear analysis will predict an unstable system near (0,0,0). Nevertheless, if interest lies in controlling unstable systems, then this sensitivity to initial conditions may not be ignored.

In order to see whether the rotation equations given above can yield a chaotic attractor with the F-15S inertia data, we solved for the above equations using a forth order Runge-Kutta scheme. To get an unstable node at (0,0,0), the aerodynamic damping terms were significantly reduced. Thus, our aerodynamic state corresponds to a stalled tail (low C_{m_q}), a shielded rudder (high AOA) and near autorotation (low C_{l_p}). These

equations will produce a chaotic attractor as is shown in figure 5.12. This figure shows the projection of the attractor in the p and q phase plane. We can see the sensibility to initial conditions by beginning near the origin but not exactly at the same location. This second solution is shown in figure 5.13. Clearly a slight change in initial conditions yields a completely different initial path to the attractor.

The above demonstrates the possibility of getting solutions to the rotations equations which are chaotic. Given that the entire equations of motion are nonlinear, we would also expect that these equations can also be chaotic (although our simulations have not yielded such solutions). The high number of degrees of freedom and the nonlinearities are the usual recipe for chaos. However, in order to achieve a chaotic solution, it is necessary to have the nonlinearities be important. In other words, small displacements of a stable system will surely not give us such motion. Yet, large diplacements or an unstable system (which will eventually yield large displacements) will eventually cause the nonlinearities to have effect. However, the problem of determining what is a small displacement still remains.

5.5 Effect of Nonlinear Aerodynamics in the Lateral Equations

As an illustration of the effects of nonlinear aerodynamics on the ensuing aircraft motion, we begin with the following lateral equations:

$$+(2\mu D - C_{y_\beta})\beta - (2\mu \sin\theta_0)\hat{p} + (2\mu \cos\theta_0)\hat{r} - (\frac{\mu bg}{VT0^2}\cos\theta_0)\phi = 0 \tag{5.20}$$

$$i_A D\hat{p} = C_{l_p}\hat{p} + C_{l_r}\hat{r} + C_{l_\beta}\beta + C_{l_{r_\beta}}\hat{r}\beta \tag{5.21}$$

$$i_C D\hat{p} = C_{n_p}\hat{p} + C_{n_r}\hat{r} + C_{n_\beta}\beta + C_{n_{r_\beta}}\hat{r}\beta \tag{5.22}$$

$$D\phi = \hat{p} + \hat{r}\tan\theta_0 \tag{5.23}$$

The roll and yaw equations now have a nonlinear term in them representing an assymetry which increases the damping with sideslip. The terms C_{y_r} and C_{y_p} were set to zero as they were for the F-15S. The data chosen corresponds to our data for the aircraft trimmed at 40 degrees AOA with the exception of C_{l_p} which was reduced to -.01745 in order to create an instability. (Our nonlinear term was made large in the plots yet smaller nonlinear terms yield similiar results.)

We solved for these equations numerically (Runge-Kutta again) and get the phase plot shown in figure 5.14 which then develops into figure 5.15. Poincare sections for β=0 (Figure 5.16) and for p=0 (Figure 5.17) show that these gyrations eventually spiral into a limit cycle. Linear analysis on the other hand will yield an unstable spiral at the origin. This solution basically corresponds to a limit cycle resembling a dutch roll motion (which is undamped);however, the bank angle oscillates between -π and -2π. Hence, our linearization of ϕ is certainly no longer valid.

Although our simplistic model yielded a limit cycle in the end, the initial nonlinear oscillations stemming from our $C_{n_{r\beta}}$ and $C_{l_{r\beta}}$ terms are significantly more complex. This demonstrates that just a few aerodynamic nonlinearities can significantly complicate the equations of motion. It is therefore extremely important that the control designer have a model which yields proper aerodynamics.

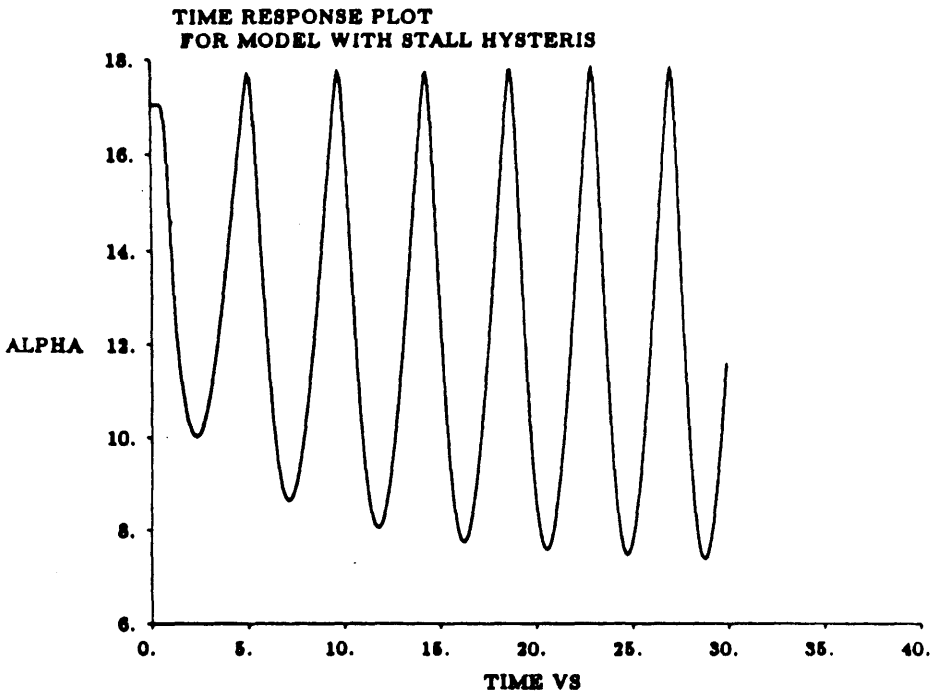

Figure 5.7: AOA time response for stall hysterisis model.

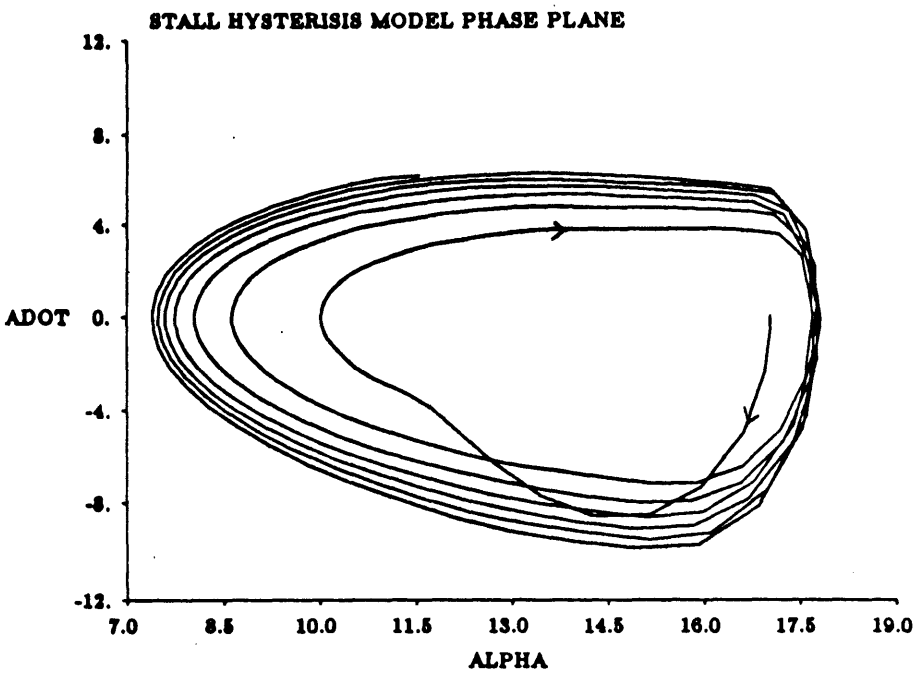

Figure 5.8: AOA phase plane for stall hysterisis model.

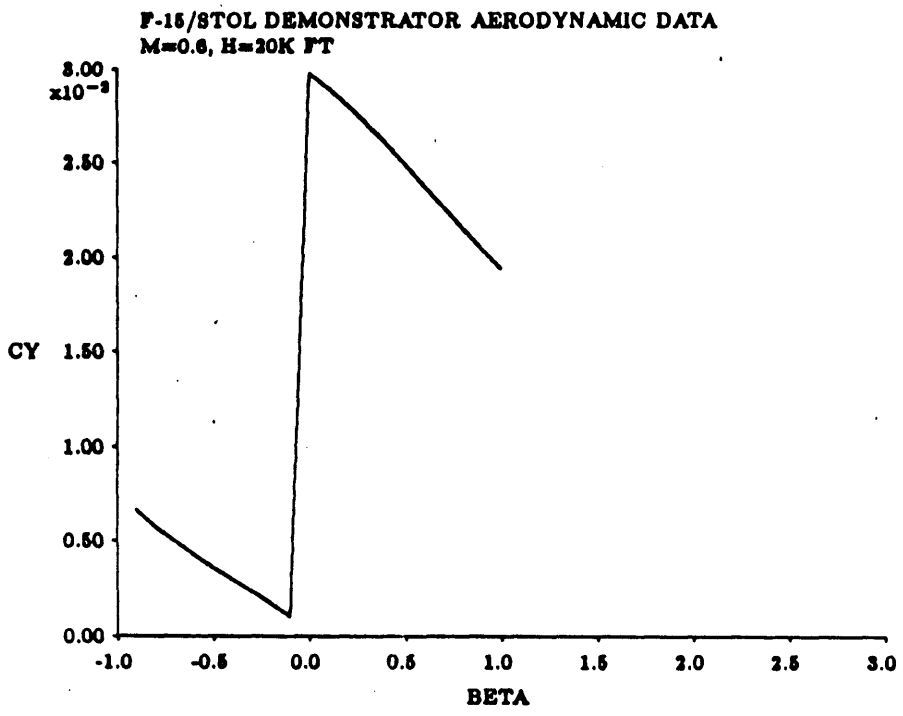

Figure 5.9: Sideforce coefficient versus Beta at alpha=40 degrees.

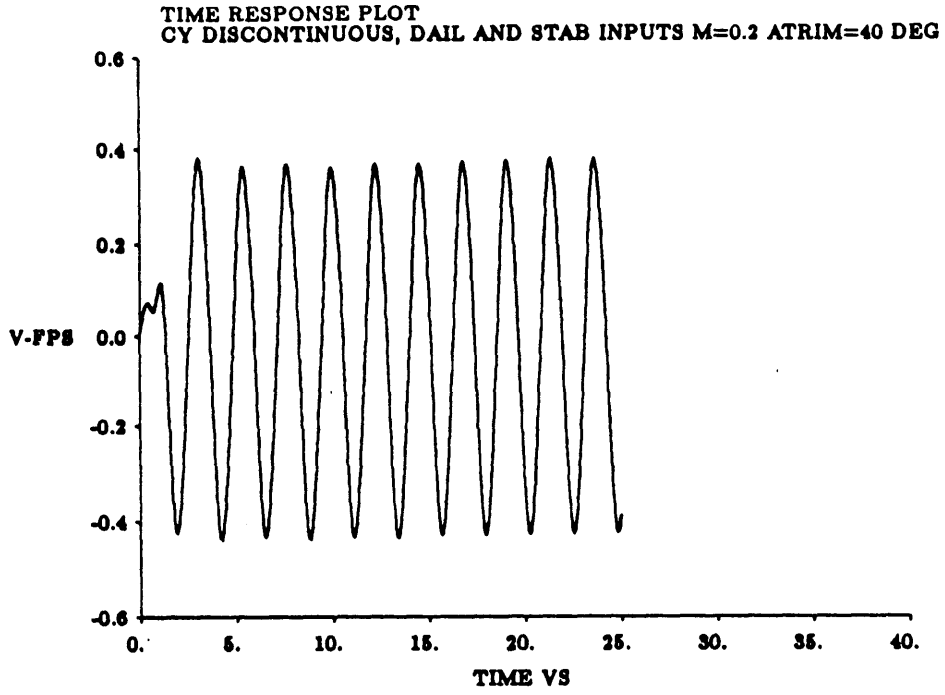

Figure 5.10: Beta time response for jump in sideforce coefficient.

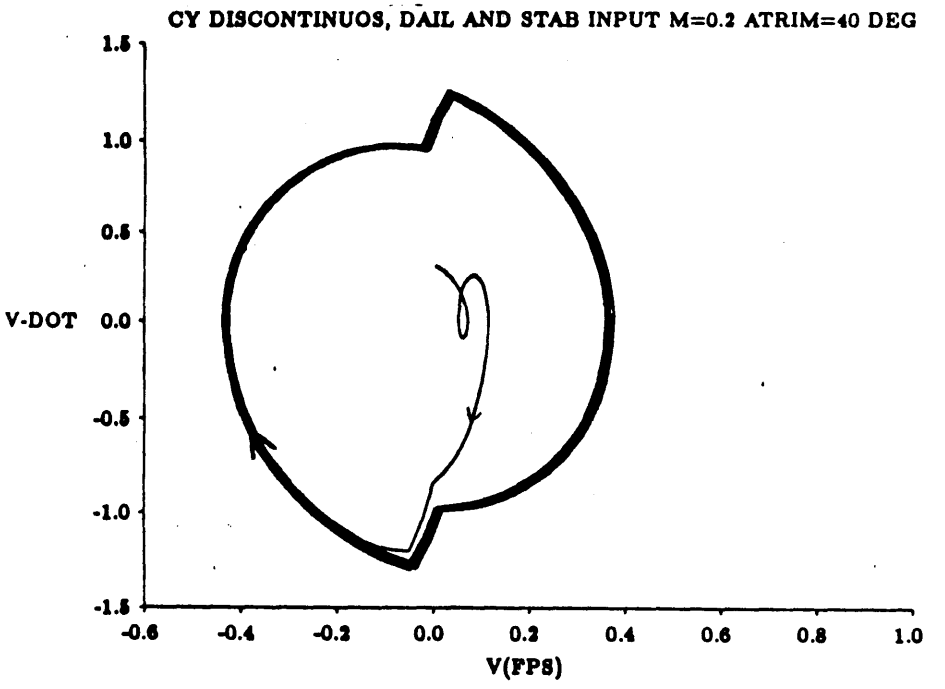

Figure 5.11: Beta phase plane

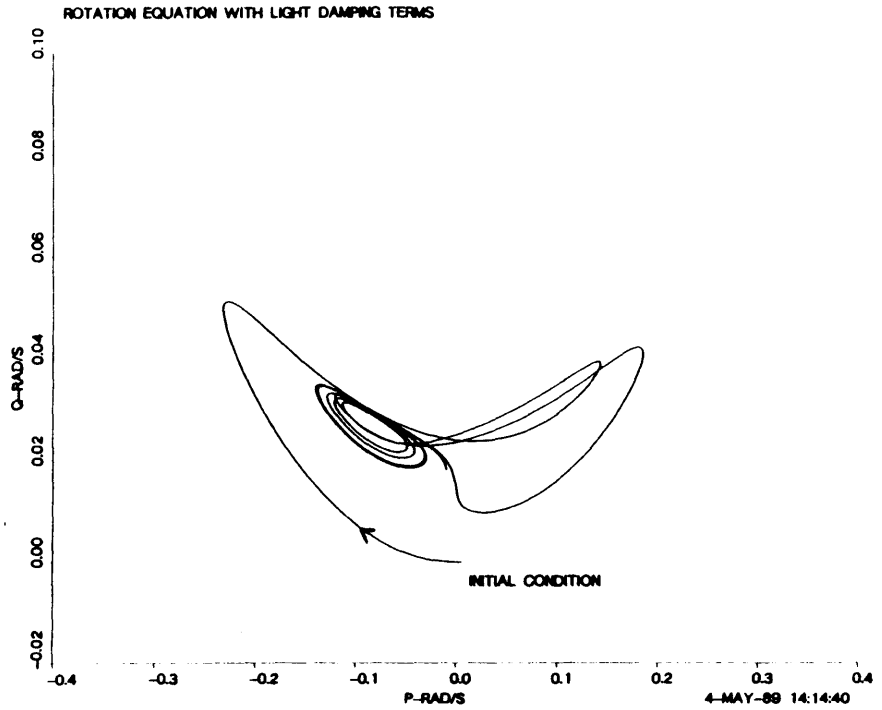

Figure 5.12: Solution to rotation equations showing strange attractor in p-q phase space.

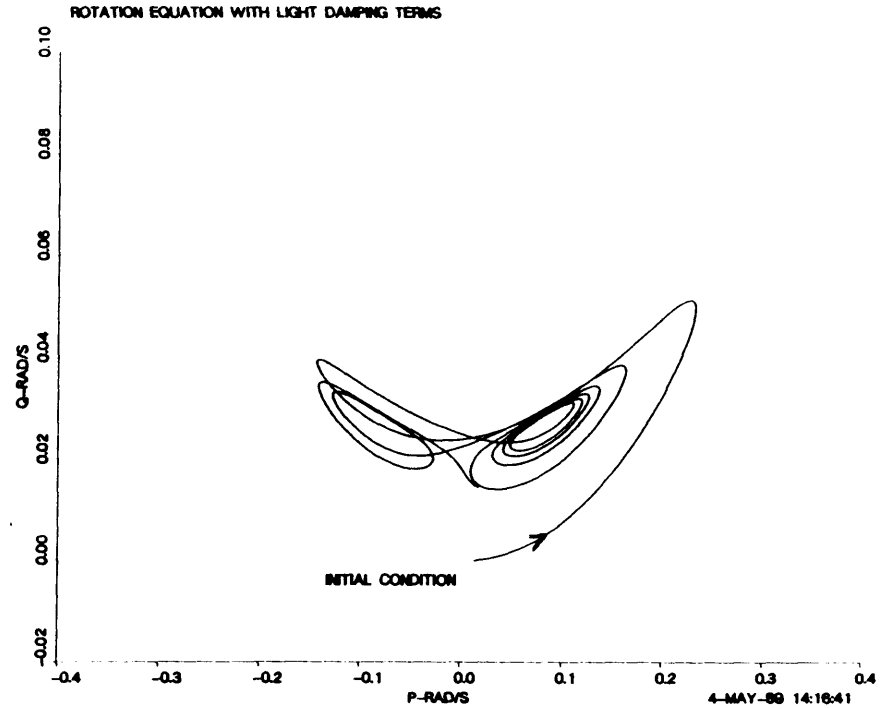

Figure 5.13: P-Q phase space for slightly perturbed initial conditions.

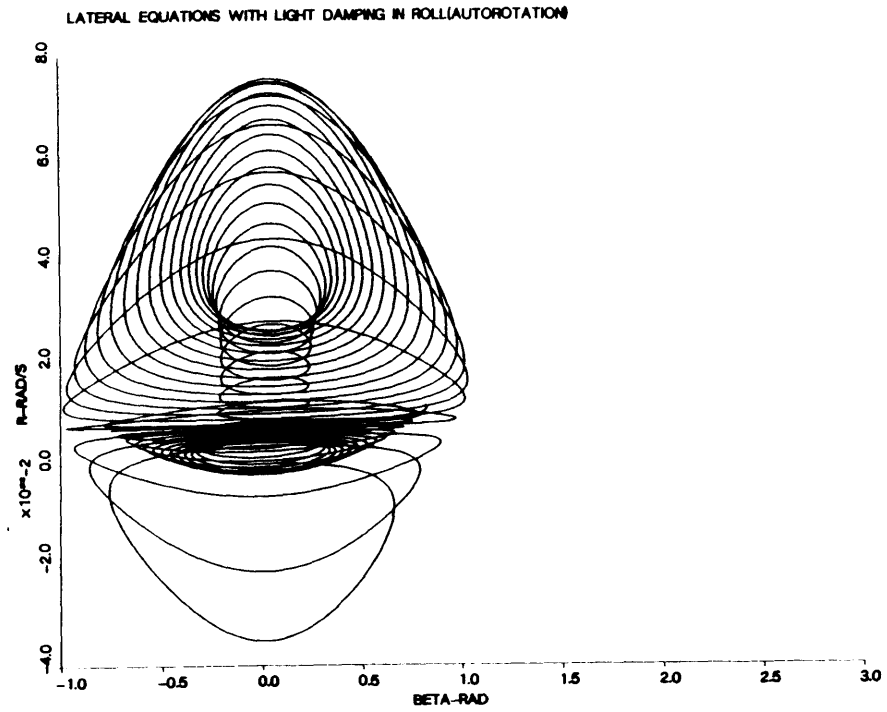

Figure 5.14: Sideslip and yaw rate phase space for nonlinear lateral eqns.

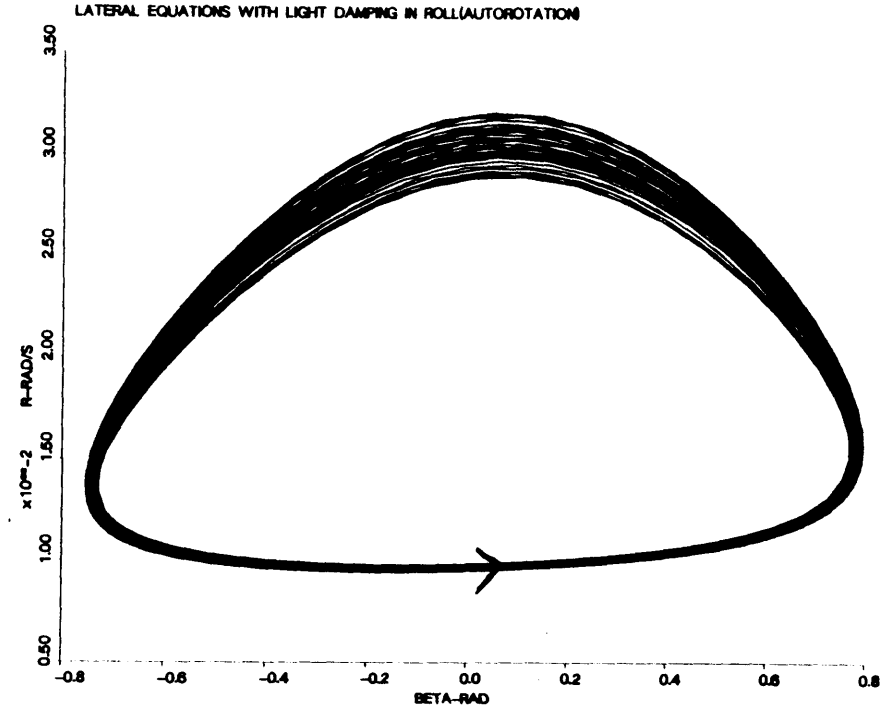

Figure 5.15: Sideslip and yaw rate phase space for nonlinear lateral eqns.

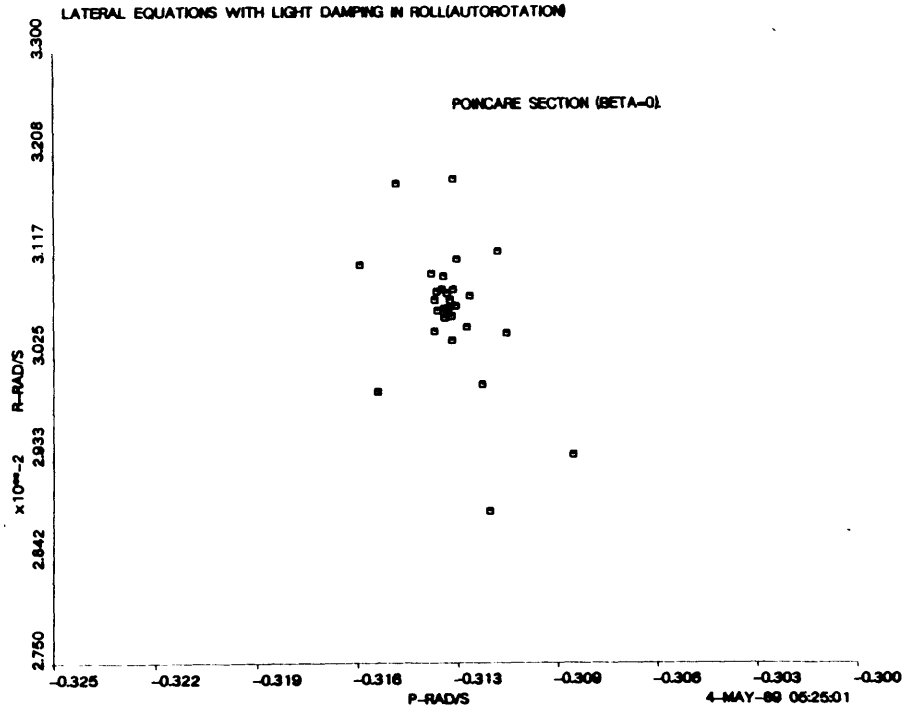

Figure 5.16: Zero sideslip poincare section.

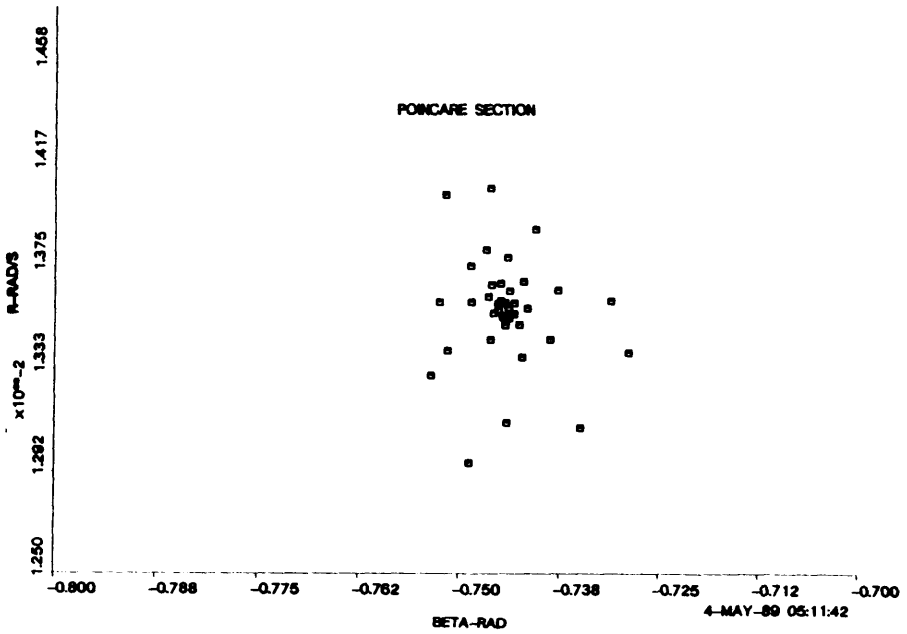

Figure 5.17: Zero roll rate poincare section.

Chapter 6

Conclusions and Recomendation for Future Work

The preceeding work has shown that the following can have strong effects on aerodynamic trajectory and dynamics:

- Cross-coupling aerodynamic terms, particularly C_{m_p}. These yield to root motion and a modification of root shapes.
- Aerodynamic lags which can modify the short period damping.
- Aerodynamic discontinuities which yield limit cycles.
- Hysterisis loops in aerodynamic parameters which cause limit cycles.
- Nonlinearities in aerodynamic forces and moments which can simply introduce higher frequencies or force an entirely chaotic solution.

Our current aircraft simulator is not equipped to properly handle some of the above situations. For instance:

- Hysterisis loops do not occur naturally from the point by point data and must be added in an *ad hoc* fashion to see the effect on the dynamics.
- Simplistic aerodynamic lag models must be incorporated to get the effect of the unsteady wake on the aircraft dynamics.

- The sparseness of points in the high angle of attack region does not capture all discontinuities.

We suggest that a better aerodynamic model be developed such as an unsteady panel method. The inclusion of separation, leading edge vortices, vortex bursting and unsteady wakes will give more proper lags, hysterisis loops, coupling derivatives and discontinuities.

Katz and Maskew (1988) recently incorporated a time dependent vortex panel method solver with an aircraft motion integrator including leading edge vortices. They found much closer lift coefficients for delta wings than previous panel solvers without leading edge separation.

Hancock and Lam (1987) also incorporated a panel solver to an aircraft motion integrator. They found differences between the panel method aerodynamic model and the fixed point stability derivative model which they believed stemmed from roll-pitch coupling due to a curved wake. Yet, they were unable to arrive at a stability derivative to account for the difference. This suggests the inadequacy of stability derivatives to account for the roll-pitch coupling.

By building on the work of the above authors, a vortex panel solver can be developed which includes; leading edge and forebody vortex separation, wing and tail stall, wing-body junction vortices and vortex bursting. Once the above model is completed, coupling this panel method to an equation of motion integrator will give the control designer a proper aircraft model around which (s)he can design a control system which will maneuver with rather than around the high angle of attack portion of the flight envelope.

Appendix A

Derivation of the Linearized Equations

The derivation of Equations 3.1 to 3.6 is given below.

A.1 Non-dimensionalization

The characteristic time used to non-dimensionalize derivatives and rotation rates was the span over twice the velocity:

$$t^* = \frac{b}{2VT0} \tag{A.1}$$

The mass and inertias were non-dimensionalized as follows:

$$\begin{aligned} \mu &= \frac{2m}{\rho S b} \\ i_A &= \frac{8I_x}{\rho S b^3} \\ i_B &= \frac{8I_y}{\rho S b^3} \\ i_C &= \frac{8I_z}{\rho S b^3} \\ i_E &= \frac{8I_{xz}}{\rho S b^3} \end{aligned} \tag{A.2}$$

The x-velocity was non-dimensionalized with the flight velocity:

$$\hat{u} = \frac{u}{VT0} \tag{A.3}$$

The y and w velocity were converted into sideslip (β) angle and angle of attack (α) respectively through:

$$\alpha = \arctan \frac{w}{u} \tag{A.4}$$

$$\beta = \arcsin \frac{v}{VT} \tag{A.5}$$

We will furthermore assume that only u,w and θ have steady state values denoted by u_0, w_0, and θ_0 , all other values denote pertubation quantities.

A.1.1 X-Equation

Beginning with:

$$\dot{u} = vr - wq + \frac{\bar{q}S}{m} C_x - g \sin\theta \tag{A.6}$$

We multiply the above by $\frac{t^*}{VT0}$ and linearize to get (note the differential operator with respect to non-dimensional time is D):

$$D\hat{u} = -\frac{w_0}{VT0}\hat{q} + \frac{VT^2}{2\mu VT0^2} C_x - \frac{gb}{2VT0^2} \sin\theta_0 + \theta \tag{A.7}$$

We note that (by linearizing):

$$\begin{aligned} \frac{VT^2}{VT0^2} &= \frac{(u_0+u)^2 + v^2 + (w_0+w)^2}{VT0^2} \\ &= 1 + 2\cos\theta\hat{u} + 2\sin\theta\frac{w}{VT0} \end{aligned} \tag{A.8}$$

From equation A.4 we can get the following:

$$\frac{w}{VT0} = \frac{\alpha}{\cos\theta_0} + \hat{u}\tan\theta_0 \tag{A.9}$$

By substituting these results into equation A.7, subtracting the steady state equation, and noting that $\hat{q} = D\theta$ we get equation 3.1.

A.1.2 Alpha Equation

Recalling equation A.4 and taking its derivative, we get:

$$\begin{aligned}\dot{\alpha} &= \frac{(u_0+u)\dot{w}-(w_0+w)\dot{u}}{(u_0+u)^2+(w_0+w)^2} \\ &= \frac{(u_0+u)\dot{w}-(w_0+w)\dot{u}}{u_0^2+w_0^2}\left(1-\frac{2u_0u+2w_0w}{u_0^2+w_0^2}\right) \\ &= \Big((\hat{u}+\cos\theta_0)\dot{\hat{w}}-(\sin\theta_0+\alpha\sec\theta_0+\hat{u}\tan\theta_0)\dot{\hat{u}}\Big) \\ &\quad (1-2\cos\theta_0\hat{u}-2\sin\theta_0(\alpha\sec\theta_0+\hat{u}\tan\theta_0)) \end{aligned} \tag{A.10}$$

Substituting the expressions for $\dot{\hat{w}}$ and $\dot{\hat{u}}$, removing nonlinear terms and subtracting the steady state equation we get the linearized equation for alpha.

A.1.3 Pitching Moment equation

From:

$$\dot{q} = \frac{\bar{q}S\bar{c}}{I_y}C_m + \left(\frac{I_z-I_x}{I_y}\right)pr + \frac{I_{xz}}{I_y}(r^2-p^2) \tag{A.11}$$

We nondimensionalize by multiplying by the square of t^*, remove nonlinear terms and expand the coefficient to get the linearized C_m equation. In the cross coupling terms, we linearized:

$$\dot{\phi} = p + \tan\theta(q\sin\phi + r\cos\phi) \tag{A.12}$$

such that:

$$\hat{p} = D\phi - \hat{r}\tan\theta_0 \tag{A.13}$$

A.1.4 Sideslip Equation

From equation A.5 we can get:

$$\dot{\beta} = \frac{\dot{v}-\sin\beta\dot{V}T}{\sqrt{(u_0+u)^2+(w_0+w)^2}}$$

$$= \frac{\dot{v}}{VT0} \tag{A.14}$$

Where we eliminated all nonlinear terms. By subsequently non-dimensionalizing the following:

$$\dot{v} = wp - ur + \frac{\bar{q}S}{m}C_y + g\cos\theta\sin\phi \tag{A.15}$$

we get an expression for $\dot{\beta}$. We must use equation A.13 to get rid of $\hat{p}$.

A.1.5 Roll and Yaw Equations

For these equations, we simply multiply the following:

$$\dot{p} = \frac{-\left(\frac{I_z - I_y}{I_x} + \frac{I_{xz}^2}{I_x I_z}\right)qr + \left(1 - \frac{I_y - I_z}{I_x}\right)\frac{I_{xz}}{I_x}pq + \frac{\bar{q}Sb}{I_x}\left(C_l + \frac{I_{xz}}{I_z}C_n\right)}{1 - \frac{I_{xz}^2}{I_x I_z}} \tag{A.16}$$

$$\dot{r} = \frac{\left(\frac{I_{xz}^2}{I_x I_z} - \frac{I_y - I_z}{I_z}\right)pq - \left(1 + \frac{I_z - I_y}{I_z}\right)\frac{I_{xz}}{I_z}qr + \frac{\bar{q}Sb}{I_z}\left(\frac{I_{xz}}{I_z}C_l + C_n\right)}{1 - \frac{I_{xz}^2}{I_x I_z}} \tag{A.17}$$

by the square of t^* and throw away the nonlinear terms (pq, qr). We can then manipulate these equations to give us yaw and roll equations as follows:

$$\begin{aligned} C_n &= i_C D\hat{r} - i_E D\hat{p} \\ C_l &= i_A D\hat{p} - i_E D\hat{r} \end{aligned} \tag{A.18}$$

Substituting equation A.13 for $\hat{p}$ and expanding the coefficients into their stability derivatives yields the linear equations.

REFERENCES

Bryan, G.H. and Williams, W.E., 'The Longitudinal Stability of Aerial Gliders', *Proc. Roy. Soc. Of London*, Vol 73, 1904, pp.101-116

Christopher, P.A.T. and Thorne, R. 'Some examples of the application of the Beecham-Tichener-Simpson (BTS) method to autonomous systems', *Aeronautical Journal*, Dec., 1985

Curry, W.H. and Orlik-Ruckemann, K.J., 'Sensitivity of Aircraft Motion to Aerodynamic Cross-Coupling at High Angles of Attack', AGARD-CP-235,*Dynamic Stability Parameters*paper 34, May 1978

Etkin, B. *Dynamics of Flight; Stability and Control* John Wiley and Sons: New York, 1982

Hancock, G.J. and Lam, J.S.Y., 'On the application of axiomatic modelling to aircraft dynamics', *Aeronautical Journal*, Jan., Feb.1987

Johnston, D.E., 'Identification of Key Maneuver-Limiting Factors in High-angle-of-attack flight', AGARD-CP-235,*Dynamic Stability Parameters* paper 36, May 1978

Katz,J. and Maskew,B. 'Unsteady Low-Speed Aerodynamic Model for Complete Aircraft Configurations', *Journal of Aircraft* vol. 25, no. 4, pp.302-310, April 1988

McCroskey, W.J. *The phenomenon of dynamic stall*, NASA TM 81264

Orlik-Ruckemann, K.J. and Hanff, E.S., 'Experiments on Cross-Coupling and Translational Acceleration Derivatives', AGARD-CP-235,*Dynamic Stability Parameters*paper 8, May 1978

Thompson, J.M.T. and Stewart,H.B. *Nonlinear Dynamics and Chaos* John Wiley and Sons: 1986

Venkatesan, C. and Friedmann,P.P. 'New Approach to Finite-State Modelling of Unsteady Aerodynamics', *AIAA Journal*,vol.24, no.12, pp.1889-1897, Dec.,1986

Wolf, J.B. *Dynamic Effects of Non-Linear Aerodynamics on a High Performance Aircraft*, M.S. Thesis 1987